

Generative design and validation of therapeutic peptides for glioblastoma based on a potential target ATP5A

Hao Qian^{1†}, Pu You^{2†}, Lin Zeng¹, Jingyuan Zhou¹, Dengdeng Huang¹,
Kaicheng Li², Shikui Tu^{1*}, Lei Xu¹

¹ Centre for Cognitive Machines and Computational Health (CMaCH), School of Computer Science, Shanghai Jiao Tong University, Shanghai, China.

²QuietD Biotech, Shanghai, China.

*Corresponding author(s). E-mail(s): tushikui@sjtu.edu.cn;

[†]These authors contributed equally to this work.

Abstract

Glioblastoma (GBM) remains the most aggressive tumor, urgently requiring novel therapeutic strategies. Here, we present a dry-to-wet framework combining generative modeling and experimental validation to optimize peptides targeting ATP5A, a potential peptide-binding protein for GBM. Our framework introduces the first lead-conditioned generative model, which focuses exploration on geometrically relevant regions around lead peptides and mitigates the combinatorial complexity of de novo methods. Specifically, we propose POTFlow, a Prior and Optimal Transport-based Flow-matching model for peptide optimization. POTFlow employs secondary structure information (e.g., helix, sheet, loop) as geometric constraints, which are further refined by optimal transport to produce shorter flow paths. With this design, our method achieves state-of-the-art performance compared with five popular approaches. When applied to GBM, our method generates peptides that selectively inhibit cell viability and significantly prolong survival in a patient-derived xenograft (PDX) model. As the first lead peptide-conditioned flow matching model, POTFlow holds strong potential as a generalizable framework for therapeutic peptide design.

Keywords: Peptide Design, Glioblastoma, Flow Matching, Generative Models

Introduction

Glioblastoma (GBM) is an aggressive brain malignancy with rapid cell proliferation, diffuse tissue invasion, and a profoundly immunosuppressive microenvironment [1, 2]. Despite standard-of-care treatments involving surgical resection followed by radiotherapy and temozolomide chemotherapy, the median survival remains approximately 15 months, with nearly universal recurrence. ATP5A, the alpha subunit and core component of mitochondrial ATP synthase’s catalytic site, has emerged as a promising therapeutic target in GBM owing to its abnormal surface localization and critical role in tumor energy metabolism [3, 4]. Targeting ATP5A in GBM presents a compelling therapeutic opportunity, yet its atypical surface exposure poses significant challenges for small-molecule drug design. Peptides offer a promising alternative, as their intermediate molecular size and structural flexibility enable them to access protein surfaces that are typically considered undruggable [5–7]. Moreover, peptides exhibit favorable pharmacological properties, including high target specificity, low immunogenicity, and cost-effective synthesis [8–10].

Traditional peptide design approaches, such as alanine scanning [11] and combinatorial screening [12], are constrained by low throughput and the combinatorial explosion of sequence variants [9, 13]. Recently, deep learning-based methods have been increasingly adopted to model protein–peptide interactions [14–19]. Besides, deep generative models, such as diffusion [20–22] and flow matching models [23, 24], have demonstrated their potential in peptide binder design [25–28].

Despite recent successes in designing peptide binders, there are still two limitations. First, current deep generative methods focus mainly on generating peptides from scratch, while in practical drug discovery, peptides are typically derived and optimized from lead sequences, as high sequence similarity often correlates with functional similarity [29]. Notably, previous studies [30, 31] elucidated the DDIT4L–TOM40–ATP5A pathway in GBM and designed a DDIT4L-derived peptide that binds ATP5A, impairs mitochondrial ATP synthase activity, and suppresses tumor growth in preclinical models. However, this ATP5A-targeting peptide essentially represents a first-generation lead obtained by motif selection, and its potency and therapeutic window remain suboptimal, underscoring the need for systematic lead optimization. Therefore, designing peptides based on lead sequences is a more reasonable and practically relevant direction. Second, the absence of experimental validation in most computational peptide design methods raises concerns about their practical applicability.

To overcome these limitations, we introduce a dry-to-wet peptide design framework for GBM. Unlike de novo methods, our framework explores the local latent space surrounding a lead peptide to identify functionally relevant candidates based on a carefully designed prior. Specifically, we propose a Prior and Optimal Transport-based Flow-matching (POTFlow) model for peptide optimization. POTFlow initializes a prior distribution using secondary structure types (e.g., helix, sheet, loop) from the lead peptide as geometric constraints. This prior is further refined via optimal transport to shift the sampling distribution closer to the lead peptide, enabling shorter flow paths and improved optimization performance. Besides, by integrating expert system filtering and experimental validation, our framework bridges in silico peptide design with wet-lab evaluation. When applied to GBM, our framework generated peptides that surpassed the lead in inhibiting cell viability in vitro and exhibited tumor cell selectivity. Moreover, it identified a candidate that significantly suppressed tumor growth in a patient-derived xenograft (PDX) model, highlighting its strong potential for therapeutic peptide design.

Methodologically, POTFlow extends multimodal flow matching from unconditional de novo generation to a lead-conditioned optimization regime. To our knowledge, POTFlow is the first lead peptide-conditioned flow-matching frameworks with integrated experimental validation, spanning in silico design, in vitro assays, and in vivo PDX models.

Results

An overview of the proposed peptide design framework for glioblastoma

We build a deep generative model jointly with experimental analysis in a dry-to-wet framework to design peptide therapeutics for GBM (Fig. 1). The core of our framework is POTFlow, the first lead-peptide-driven deep generative model, which fundamentally sets it apart from conventional de novo design methods. De novo design approaches often suffer from inefficiency and low success rates, primarily due to the vast combinatorial search space and the absence of biological context resulting from the use of an unconditional prior. In contrast, POTFlow utilizes the lead peptide to guide and restrict exploration within its local sequence–structure neighborhood (Fig. 1a–b), thereby focusing the search on geometrically relevant regions and increasing the likelihood of identifying functional candidates. These candidates are subsequently evaluated by an expert system (Fig. 1c). Top candidates are further synthesized and validated by cell viability assays and patient-derived xenograft (PDX) models (Fig. 1d). Importantly, our framework bridges computational design with experimental validation which enables efficient translation of in silico design into experimentally validated peptide therapeutics.

Here, we explain how POTFlow incorporates the lead peptide as an additional input. As illustrated in the left plot in Fig. 2b, de novo methods first sample noisy peptides from an unconditional distribution. Time-independent vector fields are then learned to transport these samples along flow matching paths toward the target peptides. POTFlow reformulates this process by conditioning the learned vector fields on the structure of a lead peptide. Instead of conditioning the model by simply appending a fixed lead-peptide embedding to all inputs, POTFlow constructs a hierarchy of lead-aware representations that modulate the flow fields at multiple geometric and sequence levels.

Firstly, we transform the unconditional residue centroids into class-specific residue centroids, where each “class” corresponds to a peptide folding type (e.g., helix, sheet, or loop) defined by the lead peptide structure (Step 1 in Fig. 2a). Here, the centroid refers to the $C\alpha$ position of each residue (see Fig. 2c for details). We show that class-specific initialization leads to shorter flow matching paths (left and center-left panels in Fig. 2b), thereby improving generation efficiency. A rigorous proof is provided in Supplementary Notes. After this step, an “improved” noisy peptide is sampled.

Secondly, we apply multimodal optimal transport (OT) between the lead peptide and the noisy peptide (Step 2 in Fig. 2a). As shown in Fig. 2c, a peptide consists of four multimodal representations, including

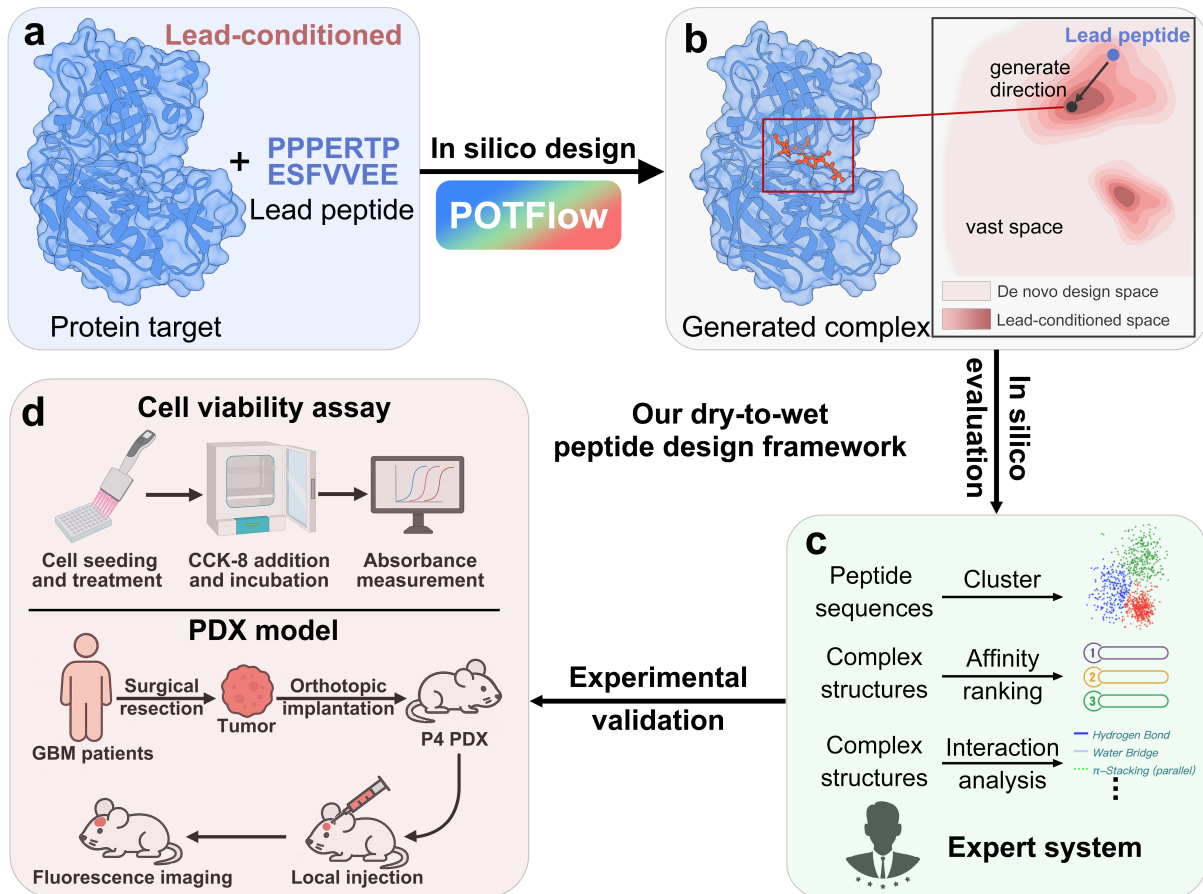


Fig. 1 Schematic workflow from in silicon peptide design to experimental validation. **a)** We start from a lead peptide sequence and 3D structure of its target protein. **b)** POTFlow efficiently samples peptide–protein complexes within the lead peptide-conditioned space. **c)** An expert system clusters candidate peptides, ranks their binding affinities, and analyzes intermolecular interactions (e.g., hydrogen bonds, water bridges, π -stacking). **d)** Promising candidates are synthesized and tested by cell-viability assays and patient-derived xenograft (PDX) models.

residue type in discrete sequence space, centroid coordinates in Euclidean space, backbone frame orientations on the $SO(3)$ manifold, and side-chain torsion angles on the torus manifold. For clarity, we only visualize the changes of residue centroid paths after OT operation (center-left and center-right panels in Fig. 2b). The OT operation can be interpreted as a permutation that reassigns noisy residues to their target counterparts, constructing more efficient pairings and minimizing the overall length of flow matching paths. Moreover, optimal transport naturally yields disentangled flow paths, facilitating more stable and efficient ODE-based generation [32]. Together, class-specific initialization and optimal transport-based residue pairing constitute a lead-conditioned scheme that guides the generation process along shorter and more disentangled flow trajectories. Our approach improves both the efficiency and stability of the ODE-based generative process, as formally justified in Supplementary Notes A.

Lastly, the aforementioned process produces paired noisy and lead peptides, which serve as anchors for the subsequent flow-based generation process. We then build a straight flow matching path by linearly interpolating within paired samples (Step 3 in Fig. 2a; rightmost panel in Fig. 2b). We refer to these procedures as Coupled Conditional Flow Matching (C²FM). Full implementation details are provided in Methods section and Supplementary Materials D.1.

We then train a neural network ϕ_θ to approximate the velocity field along the flow path. As illustrated in Fig. 2d, at an arbitrary timestep t , four residue-related variables are provided as input to ϕ_θ , which is optimized by minimizing the squared error against the lead peptide. During inference, starting from a noisy peptide sampled from the lead-conditioned initialization, we numerically integrate the corresponding ODE using the trained ϕ_θ , thereby transporting the system smoothly from noise to the desired peptide structure.

POTFlow outperforms existing methods on peptide benchmark

To evaluate our model, we curated a benchmark dataset from PepBDB [33] and Q-BioLip [34] following prior work [25, 35], yielding 8,207 training samples and 158 test complexes. We evaluate POTFlow against five

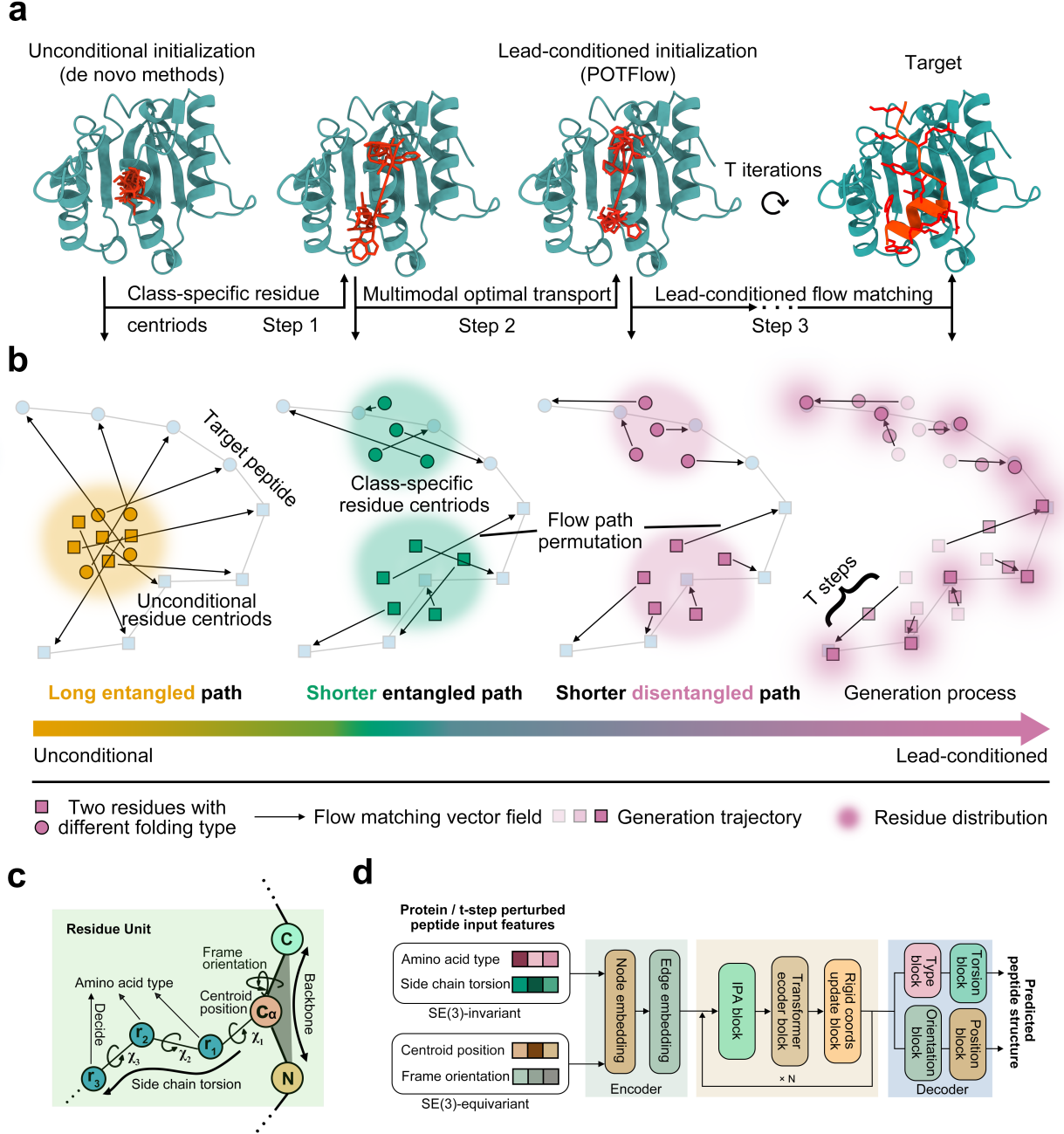


Fig. 2 **a)** An overview of **POTFlow**. First, class-specific centroids are computed from lead peptide structures. Here, “class” represents the peptide folding type (e.g., helix, sheet, loop). Next, based on the optimal transport theory, multimodal couplings between peptides and initial noise variables are established. Finally, short disentangled paths are built and lead-conditioned flow matching model generates high-affinity complex structures. **b)** Corresponding residue-level illustration of how **POTFlow** constructs more efficient generation trajectories via lead-conditioned initialization. **c)** Structural definition of a residue unit. **d)** Computational workflow of our model at t time step.

de novo generative methods, including diffusion-based models, i.e., RFDiffusion [36], ProteinGenerator [37], and PepGLAD [27], a flow matching model, PepFlow [25] and an autogressive model PepHAR [35]. De novo methods explore the complete peptide space, they often suffer from inefficiency and low success rates due to the vast combinatorial landscape and lack of biological priors. In contrast, **POTFlow** generates candidates conditioned on a lead peptide, narrowing the search to regions more likely to yield bioactive candidates. Here, classifier-guided techniques [22, 38, 39] are not considered, as they require iterative gradient-based refinement with external scoring functions. Such techniques are computationally expensive, vulnerable to biased scoring functions, and unstable during inference.

As shown in Table 1, **POTFlow** outperforms existing de novo peptide design methods across multiple evaluation metrics, demonstrating the effectiveness of its lead-conditioned generation strategy. In terms of distribution metrics, **POTFlow** achieves the highest Similarity and Compactness, indicating that it generates

Experiments	Distribution		Energy		Geometry	
	Similarity % \uparrow	Compactness % \uparrow	Affinity % \uparrow	Stability % \uparrow	RMSD \AA \downarrow	BSR % \uparrow
RFDiffusion	46.26	74.61	16.53	26.82	4.17	26.71
ProteinGenerator	47.61	77.43	13.47	23.84	4.35	24.62
PepFlow	49.74	79.77	21.37	18.15	2.07	86.89
PepGLAD	24.93	67.90	10.47	20.39	3.83	19.34
PepHAR	20.89	70.42	20.53	16.62	2.68	86.74
Vanilla	32.20	72.71	18.37	21.89	2.44	79.0
POTFlow w/o class prior	51.96	94.61	24.21	23.12	1.77	86.03
POTFlow w/o OT	49.75	81.13	25.62	26.35	1.85	87.10
POTFlow	53.44	95.07	30.56	23.80	1.66	87.01

Table 1 Comparison of five de novo peptide design methods and three POTFlow variants on peptide benchmark. Bold values denote the best performance for each metric.

peptides structurally and sequentially closer to the lead peptide while maintaining a highly concentrated distribution in the latent space. This advantage results from the proposed C²FM technique, which effectively restricts the sampling process to a focused region around the lead peptide.

For energy metrics, POTFlow attains the highest Affinity score, reflecting its superior capability in generating peptides with stronger predicted binding to the target protein. In terms of geometric quality, POTFlow obtains the lowest RMSD, confirming its precision in producing structurally accurate peptide conformations. These improvements are attributed to the integration of class-specific priors and optimal transport-based residue pairing, which collectively construct shorter, disentangled flow paths for generation. POTFlow also achieves a high binding site rate (BSR), which measures the overlap between generated and native peptide binding interfaces. This highlights the effectiveness of lead-conditioned generation in capturing geometrically relevant interactions overlapping with the binding mode of lead peptides. For detailed metric definitions, please refer to the Methods section.

Ablation studies highlight the effectiveness of POTFlow

The last four rows of Table 1 present an ablation study of POTFlow, testing different variations and configurations of the model to assess their impact on various performance metrics. When class priors are removed (POTFlow w/o class prior), there is a noticeable drop in performance, especially for the affinity metric. Similarly, the removal of optimal transport policy (POTFlow w/o ot) also leads to reduced performance, particularly in terms of compactness and similarity metrics. When both class priors and optimal transport policy are removed (Vanilla), the performance drops to the worst across most metrics.

We further divide the peptides into four groups based on the number of secondary structures and compute the RMSD metric. As shown in Fig. 3a, POTFlow without optimal transport (w/o OT) consistently achieves lower RMSD values than the vanilla model across all groups. Notably, we observe a progressive reduction in RMSD as the number of secondary structure classes increases. This trend reflects the fact that more classes yield more informative priors, leading to shorter and more efficient flow matching paths, thereby improving model performance (Proposition 2 in Supplementary Notes A). Similarly, POTFlow without class priors also outperforms the vanilla model in all groups. Together, these results highlight that both optimal transport and class-specific priors are essential for improving overall performance (Theorem 3 in Supplementary Notes A).

Additionally, we plot the Ramachandran [41] figure for both generated peptides and lead peptides. This plot illustrates the distribution of backbone dihedral angles ψ and ϕ , which are key determinants of protein conformation and folding behavior. As shown in Fig. 3b, the ϕ - ψ angle distribution of the generated candidates closely matches that of the lead peptides, indicating realistic backbone conformations.

Optimization of the ATP5A-binding lead peptide via POTFlow

Recent work by You et al. [31] delineated the DDIT4L-TOM40-ATP5A pathway as an endogenous brake on GBM oncogenesis and showed that a DDIT4L-derived peptide (DDIT4L^{V125-P132}) targeting ATP5A

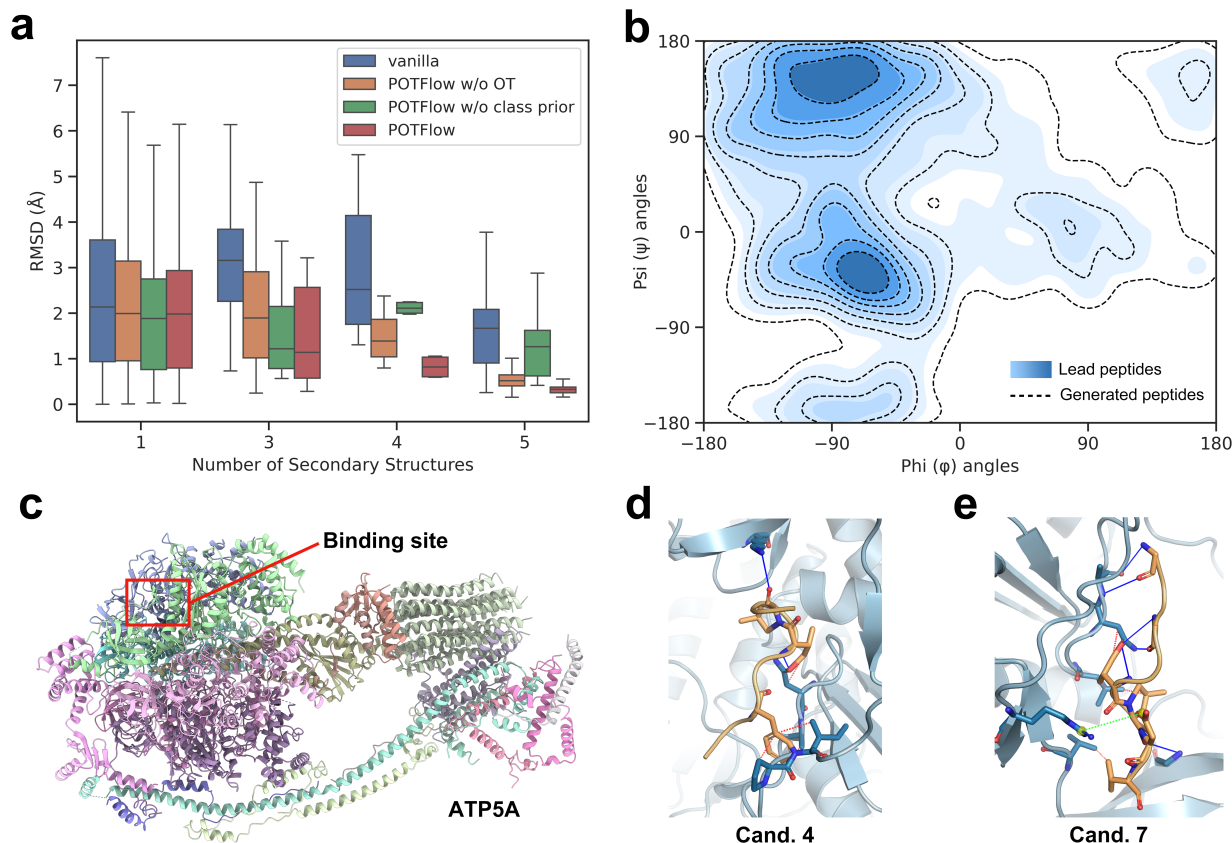


Fig. 3 **a)** RMSD values on different number of secondary structures across four models. The RMSD values are computed between generated peptides and the lead peptides in the test set. **b)** Ramachandran plot of POTFlow generated and lead peptides. **c)** Visualization of the ATP5A subunit. The red box indicates the experimentally validated peptide-binding site used as the input for subsequent generative modeling. **d-e)** Detailed non-covalent interactions of two generated candidates with protein ATP5A, as identified by the Protein-Ligand Interaction Profiler (PLIP) [40]. Hydrogen bonds are shown as blue solid lines, hydrophobic contacts as red dashed lines, and salt bridges as green dashed lines.

can impair mitochondrial ATP synthase activity, induce GBM cell apoptosis, and suppress tumor growth in orthotopic PDX models. However, this ATP5A-binding peptide represents only a first-generation lead obtained by motif selection, and its sequence space and therapeutic window remain largely unexplored. In this study, we aim to optimize this existing ATP5A-binding lead peptide using our geometry-aware generative framework POTFlow. As described below, POTFlow transforms this suboptimal lead into structurally diverse candidates and identifies peptides that not only enhance cell viability inhibition and tumor selectivity in vitro but also significantly reduce tumor burden and prolong survival in a GBM PDX model.

Rapid design and screening of peptides for GBM in silico

Starting from the lead peptide sequence which binds to ATP5A within a pocket (Fig. 3c), we employed our framework to further optimize this candidate. Specifically, given the 3D structure of ATP5A and the lead peptide sequence, we initialize peptide-protein binding conformations using AlphaFold 3. Based on these conformations, POTFlow performs lead-conditioned flow matching in a learned latent space to efficiently explore the local structural neighborhood of the lead. This process yields 2,985 unique peptide candidates with binding modes informed by the original lead. To bridge generative modeling and experimental validation, we implemented a multi-dimensional expert system that leverages sequence similarity, predicted affinity, and interaction profiles to navigate the lead-conditioned design space constructed by POTFlow. First, we clustered the peptides into 15 groups using GibbsCluster [42], and selected the group whose representative sequence exhibited the highest similarity to the lead peptide. Within this group, we then evaluated 110 peptides in terms of predicted binding affinity and peptide-protein interaction profiles. Based on this integrative assessment, seven candidates were finally selected for downstream experimental validation.

To explore the binding potential of POTFlow-generated peptides, we visualized two candidates for their interaction profiles. As shown in Fig. 3d-e, Cand. 4 engages the binding site through three hydrogen bonds

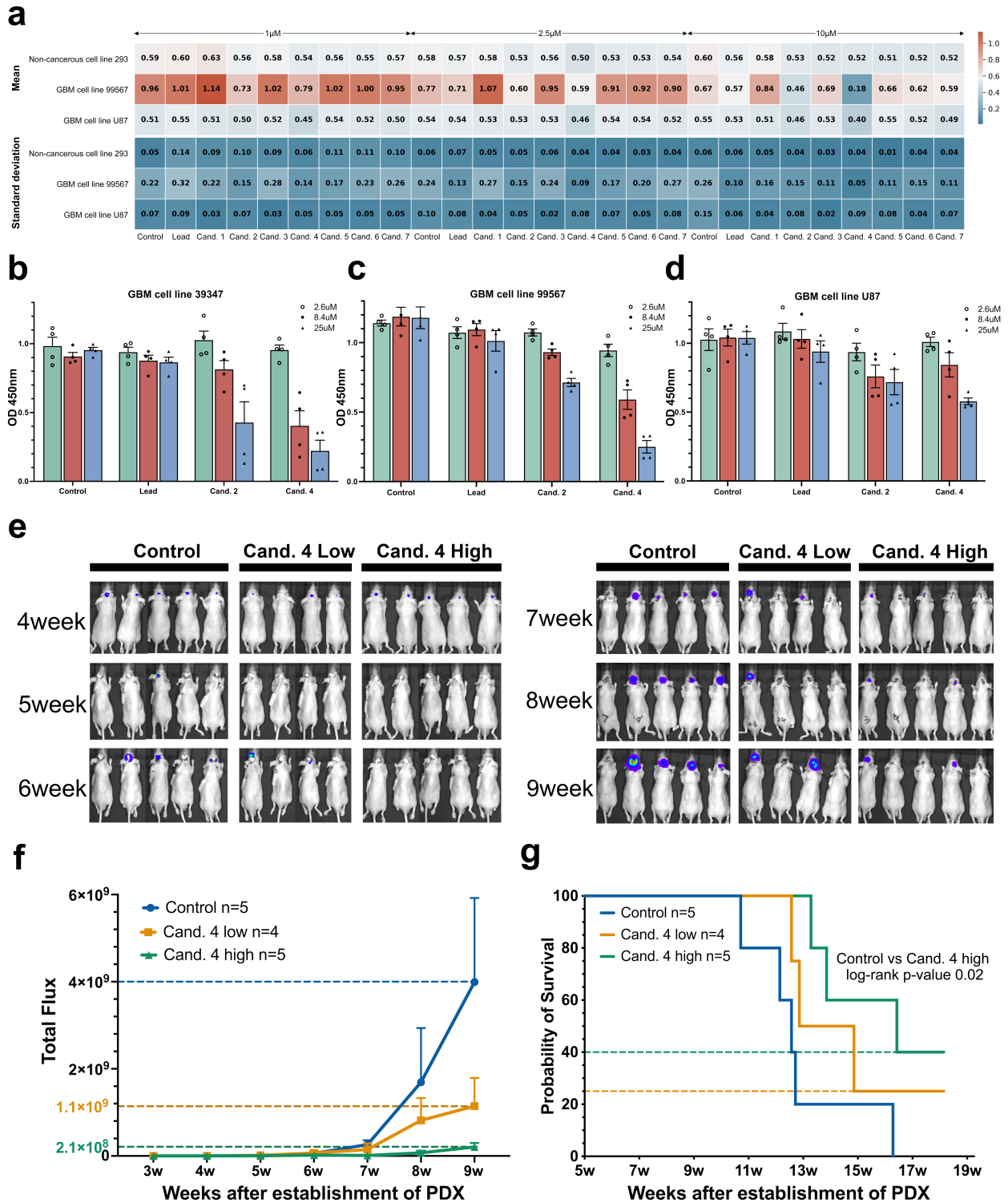


Fig. 4 **a**): Heatmap of cell viability (mean \pm SE) in GBM and non-cancerous cells. Cells from non-cancerous cell line 293 and two GBM patient-derived lines (99567 and U87) were treated with control, a reference lead peptide, and seven candidate peptides (Cand. 1–7) at three concentrations (1 μ M, 2.5 μ M, and 10 μ M). Viability was measured by CCK-8 assay and normalized to the control for each cell line. The upper panel shows the mean normalized viability, and the lower panel displays the corresponding standard deviation across nine independent experiments. Color intensity reflects relative viability (blue = lower, red = higher). **b–d**): Cell viability of GBM cell lines (39347, 99567 and U87 respectively) with control, a lead peptide, Cand. 2 and Cand. 4 at 2.6 μ M (open circles), 8.4 μ M (filled circles) and 25 μ M (triangles). The y-axis represents absorbance at 450 nm. **e**) Bioluminescence imaging of tumor progression in mice under different treatment conditions. Images were taken weekly from week 4 to week 9. **f**) In vivo bioluminescence imaging of PDX mice following local delivery of Cand. 4 via subcutaneous minipumps. Mice received either control (blue circles, $n = 5$, 10mg/kg), low-dose Cand. 4 (yellow squares, $n = 4$, 10mg/kg), or high-dose Cand. 4 (green triangles, $n = 5$, 20mg/kg). **g**) Kaplan–Meier survival curves of PDX mice treated with the same regimens. Survival was monitored daily after tumor establishment. Here, n indicates the number of mice per group.

and two hydrophobic contacts, while Cand. 7 exhibits a denser interaction network including five hydrogen bonds, three hydrophobic contacts, and a stabilizing salt bridge. These visualizations suggest that POTFlow-generated peptides can establish diverse and potentially stable non-covalent interactions with the target.

Improved cell viability inhibition and tumor selectivity of generated peptides

Seven candidates were evaluated for their ability to inhibit cell viability in three different cell lines. These candidates were tested at three concentrations (1, 2.5, and 10 μ M) on two GBM cell lines (99567 and U87) and one non-cancerous cell line (293). Cell viability was quantified using Cell Counting Kit-8 (CCK-8) assay. This colorimetric method measures mitochondrial dehydrogenase activity in viable cells, with lower absorbance values at 450 nm indicating reduced cell viability and increased peptide-induced cytotoxicity.

Fig. 4a shows the detailed inhibitory effects of the candidates across all cell lines and concentrations after 24 hours of treatment. Our candidates showed stronger inhibition of cell viability compared to the lead peptide in most of the test conditions. Notably, Cand. 2 and Cand. 4 showed strongest inhibitory effects than the other candidates. We further validated the inhibitory effects of Cand. 2 and Cand. 4 on tumor cells under higher seeding density conditions. As shown in Fig. 4b–d, both candidates effectively suppressed the viability of all three GBM cell lines after 24 hours of treatment. In addition to reduced cell viability, they also led to decreased intracellular ATP levels, indicating potential inhibition of ATP synthase activity (Supplementary Fig. 5). These results highlight the robustness of POTFlow in lead-conditioned peptide design.

To evaluate peptide selectivity, we calculated the inhibition of viability rate (IVR):

$$\text{IVR} = \frac{\text{Viability}_{\text{Lead}} - \text{Viability}_{\text{Candidate}}}{\text{Viability}_{\text{Lead}}} \times 100\%.$$

Notably, Cand. 4 exhibited a significantly higher inhibitory rate in GBM cells (18~68%) than in non-cancerous cell (less than 10%, Supplementary Table 2). These results highlight that our framework not only enhances cell viability inhibition but also yields candidates with improved specificity toward GBM cells.

Improved tumor suppression by peptide candidate 4 in the PDX model

We established a GBM PDX model by orthotopically implanting luciferase-labeled, patient-derived tumor-initiating cells into immunocompromised mice. Cand. 4, which most effectively suppressed tumor cell viability in vitro, was administered intracranially by osmotic pumps (ALZET®, 1002) to direct deliver the peptide or control peptide (dissolved in PBS) to the injection site 4 weeks after intracranial tumor cell injection. Tumor progression was monitored weekly via in vivo bioluminescence using the IVIS Lumina II system.

As shown in Fig. 4e–f, high-dose Cand. 4 treatment (20mg/kg) led to a marked suppression of tumor growth in PDX mice, with bioluminescent signals remaining low throughout the 11-week observation period. By contrast, mice in control group exhibited exponential tumor expansion beginning at week 7, whereas the low-dose group (10mg/kg) displayed a moderate inhibitory effect. Survival analysis further revealed that all control mice succumbed by week 16, while 25% and 40% of mice in the low- and high-dose groups, respectively, survived beyond week 18 (Fig. 4g). Notably, high-dose Cand. 4 significantly improved survival compared to control (p -value = 0.02, Supplementary Table 3). These results demonstrate the in vivo efficacy of Cand. 4 and highlight its potential as a therapeutic peptide for GBM.

Discussion

In this study, we present a dry-to-wet peptide design framework for GBM. Rather than generating peptides from scratch, our model POTFlow adopts a lead-conditioned scheme to guide generation. By leveraging the lead peptide, POTFlow efficiently explores its local sequence–structure space to produce candidates with enhanced therapeutic potential. We validated the framework in both cellular and PDX models, demonstrating its ability to generate peptides with tumor selectivity in vitro and therapeutic efficacy in vivo. Although POTFlow was applied to generate peptides only for GBM in this study, it can be readily adapted to other diseases by providing the corresponding target protein and the lead peptide.

While POTFlow achieves state-of-the-art performance in our benchmarks, several opportunities for further improvement remain. First, the current framework does not explicitly consider peptide properties, such as solubility and metabolic stability, which are critical for practical application. Second, while our approach is validated through both computational and experimental evaluations, the current workflow lacks an iterative feedback mechanism: experimental results are not yet integrated into the generative process to guide subsequent optimization. Third, while we observed ATP depletion and robust anti-tumor effects in vitro and in vivo, we have not yet directly visualized changes in ATP5A subcellular localization (e.g., by IF) or

fully dissected the in vivo mechanism beyond survival and tumor burden. These aspects represent promising directions for improving the performance and robustness of our framework.

In summary, we present the first generalizable framework for lead-conditioned peptide design with experimental validation. Our approach outperforms the lead peptide in inhibiting cell viability in vitro and demonstrates in vivo efficacy in a PDX model. Combined with its adaptability to diverse targets, our framework offers a promising platform for therapeutic peptide design.

Materials and Methods

Notations

Protein-peptide complexes are represented as $\mathcal{C} = \{\mathcal{P}, \mathcal{G}\}$ consisting of protein \mathcal{P} and peptide \mathcal{G} , both of which can be decomposed as residue frames. The geometric structure of the i -th residue is parameterized with C_α coordinate $\mathbf{x}^{(i)} \in \mathbb{R}^3$ and a frame orientation matrix $\mathbf{o}^{(i)} \in SO^3$ following AlphaFold 3 [43]. We define i -th residue side-chain angles as $\chi^{(i)} = \{\chi_1^{(i)}, \chi_2^{(i)}, \chi_3^{(i)}, \chi_4^{(i)}, \chi_5^{(i)}\}$ and its residue type as $\mathbf{c}^{(i)} \in \mathbb{R}^{20}$. As a result, a protein/peptide consisting of N residues can be represented as $\{\mathcal{R}^{(i)}\}_{i=1}^N$, where $\mathcal{R}^{(i)} = \{\mathbf{x}^{(i)}, \mathbf{o}^{(i)}, \chi^{(i)}, \mathbf{c}^{(i)}\}$.

The Overview of POTFlow

Given a target protein pocket \mathcal{P} and a lead peptide \mathcal{G}_l , the task of POTFlow is to design new peptides \mathcal{G} that not only bind effectively to the target protein but also closely resemble the lead peptide. Mathematically, the objective of POTFlow is to learn the dual-conditioned distribution $p_\theta(\mathcal{G} | \mathcal{P}, \mathcal{G}_l)$ which can empirically be decomposed into four independent components:

$$p(\mathcal{G} | \mathcal{P}, \mathcal{G}_l) \propto p(\{\mathbf{x}^{(i)}\}_{i=1}^N | \mathcal{P}, \mathcal{G}_l) \cdot p(\{\mathbf{o}^{(i)}\}_{i=1}^N | \mathcal{P}, \mathcal{G}_l) \cdot p(\{\chi^{(i)}\}_{i=1}^N | \mathcal{P}, \mathcal{G}_l) \cdot p(\{\mathbf{c}^{(i)}\}_{i=1}^N | \mathcal{P}, \mathcal{G}_l).$$

Our approach differs from previous methods [25–28, 35] by incorporating an additional condition based on the lead peptide, which enhances practicality in real-world peptide design. To effectively integrate this new variable, we introduce two techniques to address our objective: 1) constructing the prior distribution of residue centroids based on the secondary structure of the lead peptide; 2) applying a multimodal optimal transport policy to the initialized noisy residues for shorter and disentangled flow matching paths. We name the integration of Conditional Flow Matching with the coupling technique as C²FM.

Prior distribution of residue centroids

The secondary structure of a peptide plays a pivotal role in determining its biological function, structural stability, and binding interactions with target proteins [44–46]. To incorporate this key biological insight into our generative process, we leverage secondary structure annotations derived from the DSSP algorithm, implemented via the Biopython library [47]. Each residue in the lead peptide is assigned to a structural class, such as helix, sheet, or loop. The complete mapping is summarized in Supplementary Table 1.

To initialize the 3D coordinates of backbone C_α atoms in a biologically meaningful way, we construct a prior distribution conditioned on the secondary structure class of each residue. Specifically, for each structural class, we compute the average 3D position (centroid) of the residues assigned to that class in the input structure. These centroids serve as class-specific anchors. The new initial positions are then sampled from a normal distribution centered at the corresponding centroid, ensuring that the structural context is preserved during initialization.

This strategy contrasts with an unconditional initialization approach, which treats all residues identically (i.e., “global initialization”). We found that using class-specific centroids leads to a more accurate reconstruction of the original geometry, as it reduces the average deviation between initialized and reference coordinates. Moreover, this sampling process is equivariant to rotation. That is, if the input structure is rotated in 3D space, the initialized positions will rotate in a consistent manner. This property is essential for preserving the geometric integrity of protein-peptide complexes during downstream modeling. Further details are provided in Supplementary Notes A and Supplementary Fig. 1.

Multimodal C²FM technique

Each peptide can be described as a sequence of N residues, where each residue has four main features: C_α position, backbone orientation, side-chain torsion angles, and amino acid type. These features lie in distinct geometric spaces, making peptide modeling a multimodal problem. Below, we introduce our approach for each component within the C²FM framework.

C²FM for C_α positions

The 3D coordinates of the C_α atoms form the backbone scaffold of a peptide. We denote the position of the i -th residue as $\mathbf{x}^{(i)} \in \mathbb{R}^3$, and collectively as $\mathbf{X} = \{\mathbf{x}^{(i)}\}_{i=1}^N$. Initial positions are sampled from a class-conditional Gaussian prior informed by secondary structure annotations (Supplementary Eq. 18). A continuous flow is then trained to transform these noisy initializations \mathbf{X}_0 toward ground-truth structures \mathbf{X}_1 by learning the velocity field along a linear interpolation:

$$\mathbf{X}_t = (1 - t) \mathbf{X}_0 + t \mathbf{X}_1, \quad (1)$$

where $t \in [0, 1]$. A neural network v_t^{pos} is trained to minimize the flow-matching loss between predicted and true velocity fields $\mathbf{X}_1 - \mathbf{X}_0$.

To better align \mathbf{X}_0 with \mathbf{X}_1 , we introduce a structure-aware optimal transport [48, 49] (OT) step. OT provides a principled way to find a minimal-cost assignment between two sets of points under a given distance metric. In our case, the cost is defined as the squared Euclidean distance between C_α positions, and the transport is constrained to occur only within the same secondary structure class.

Formally, we solve a constrained OT problem to obtain a discrete permutation Π^{pos} that minimizes the total transport cost:

$$W_2(\mathbf{X}_0, \mathbf{X}_1) = \sum_{i,j} \Pi_{i,j}^{pos} \left\| \mathbf{x}_0^{(i)} - \mathbf{x}_1^{(j)} \right\|^2. \quad (2)$$

This yields a reassigned initialization $\mathbf{X}'_0 \sim \Pi^{pos}(\mathbf{X}_0, \mathbf{X}_1)$ that provides shorter and more stable flow trajectories during training. The OT solution is efficiently computed using the Python Optimal Transport (POT) library [50], benefiting from the limited length of peptide sequences (typically $N < 25$). Unlike previous work [32], which applies OT between samples to improve inter-sample flow trajectories, our approach performs OT within each individual peptide, i.e., intra-sample flow trajectories.

During inference, new C_α positions are generated by numerically integrating the learned velocity field starting from \mathbf{X}'_0 using forward Euler steps:

$$\mathbf{X}'_{t+\Delta t} = \mathbf{X}'_t + \Delta t \cdot v_t^{pos}(\mathbf{X}'_t; \theta). \quad (3)$$

C²FM for frame orientations

We represent the orientation of i -th residue as a rotation matrix $\mathbf{o}^{(i)} \in SO(3)$, with the full set denoted as $\mathbf{O} = \{\mathbf{o}^{(i)}\}_{i=1}^N$. Unlike Euclidean space, $SO(3)$ is a curved manifold, making standard linear interpolation inapplicable. To generate smooth and valid orientation trajectories, we construct geodesic flows on $SO(3)$ using operations in its Lie algebra. Initial orientations $\mathbf{o}_0^{(i)}$ are sampled uniformly from $SO(3)$, and $\mathbf{o}_1^{(i)}$ are taken from ground-truth structures.

We define the flow path as the geodesic between the two rotations:

$$\mathbf{O}_t = \exp_{\mathbf{O}_0} (t \cdot \log_{\mathbf{O}_0}(\mathbf{O}_1)), t \in [0, 1]. \quad (4)$$

To reduce path length and improve flow stability, we compute an optimal transport permutation Π^{ori} that minimizes the total transport cost on Riemannian manifold:

$$W_{so(3)}(\mathbf{O}_0, \mathbf{O}_1) = \sum_{i,j} \Pi_{i,j}^{ori} \left\| \log_{\mathbf{o}_0^{(i)}}(\mathbf{o}_1^{(j)}) \right\|^2. \quad (5)$$

This results in a permuted initialization $\mathbf{O}'_0 \sim \Pi^{ori}(\mathbf{O}_0, \mathbf{O}_1)$ that more closely aligns with the target orientations. A neural network v_t^{ori} is then trained to predict the geodesic velocity vector $\log_{\mathbf{O}'_0}(\mathbf{O}_1)$ along the path.

During generation, we apply geodesic Euler updates:

$$\mathbf{O}'_{t+\Delta t} = \exp_{\mathbf{O}'_t} (\Delta t \cdot v_t^{ori}(\mathbf{O}'_t; \theta)). \quad (6)$$

C²FM for residue types

The amino acid types in a peptide can be denoted as $C = \{c^{(i)}\}_{i=1}^N$ where $c^{(i)} \in \{c \in \mathbb{Z}^+ \mid 1 \leq c \leq 20\}$. Here, we utilize a soft one-hot technique to map discrete $c^{(i)}$ into continuous one by $\text{onehot}_{\text{soft}}(c^{(i)}) = \mathbf{s}^{(i)} \in \mathbb{R}^{20}$,

and the j -th value in $\mathbf{s}^{(i)}$ is defined as follows:

$$s^{(i)}[j] = \begin{cases} K, & j = c^{(i)} - 1 \\ -K, & j \neq c^{(i)} - 1 \end{cases}, \quad (7)$$

where K is a constant. Here, $\mathbf{s}^{(i)}$ is treated as the logits of probabilities, and $\text{softmax}(\mathbf{s}^{(i)})$ represents the normalized distribution of residue types, where the $(c^{(i)} - 1)$ -th term closes to 1 and others close to 0. This means that $\text{softmax}(\mathbf{s}^{(i)})$ is a data point in 20-category probability simplex Δ^{19} . We initialize $\mathbf{s}^{(i)} \sim \mathcal{N}(0, K^2 I)$ so that the prior distribution on simplex becomes the logistic-normal distribution [51, 52].

The flow path is defined as a linear interpolation in logit space:

$$\mathbf{s}_t^{(i)} = (1 - t) \mathbf{s}_0^{(i)} + t \mathbf{s}_1^{(i)}, t \in [0, 1]. \quad (8)$$

To better align initial and target residue distributions, we apply an optimal transport permutation Π^{type} that minimizes the total cross-entropy cost between logit vectors:

$$W_{CE}(\mathbf{S}_0, \mathbf{S}_1) = \sum_{i,j} \Pi_{i,j}^{type} \text{CE}(\mathbf{s}_0^{(i)}, \mathbf{s}_1^{(j)}), \quad (9)$$

where $\text{CE}(\cdot, \cdot)$ denotes the cross-entropy between initial and true logits. The permuted initialization $\mathbf{S}'_0 \sim \Pi^{type}(\mathbf{S}_0, \mathbf{S}_1)$ is used to train the neural network v_t^{type} to approximate the logit velocity vector $\mathbf{S}_1 - \mathbf{S}'_0$.

During inference, we integrate the learned velocity in logit space and decode residue types as follows:

$$\mathbf{C}'_{t+\Delta t} \sim \text{softmax}(\mathbf{S}'_t + \Delta t \cdot v_t^{type}(\mathbf{S}'_t; \theta)), \quad (10)$$

$$\mathbf{S}'_{t+\Delta t} = \text{onehot}_{\text{soft}}(\mathbf{C}'_{t+\Delta t}). \quad (11)$$

C²FM for side-chain torsions

Each residue i has a set of side-chain torsion angles $\mathcal{X}^{(i)} = \{\chi^{(i,j)}\}_{j=1}^{N_i}$, where $N_i \in \{1, 2, 3, 4, 5\}$ depends on the residue type. Due to the periodic nature of torsional rotations, the side-chain angles $\chi^{(i,j)}$ are defined on the torus with periodicity 2π (or π when rotational symmetry applies). Mathematically, the torsion vector $\mathcal{X}^{(i)}$ lies in the 5-dimensional torus manifold \mathbb{T}^5 which can also be interpreted as the quotient space $\mathbb{R}^5 / (2\pi\mathbb{Z}^5)$. Exponential and logarithm maps on this Riemannian manifold are similar to those in Euclidean space, with the main difference being the equivalence relation that identifies elements differing by integer multiples of 2π .

We initialize $\mathcal{X}_0^{(i)}$ from the uniform distribution over $[0, 2\pi)^{N_i}$ and define the flow path via wrapped linear interpolation:

$$\mathcal{X}_t^{(i)} = (t\mathcal{X}_1^{(i)} + (1 - t)\mathcal{X}_0^{(i)}) \bmod 2\pi. \quad (12)$$

We construct an optimal transport permutation Π^{ang} using a cosine distance metric. Specifically, we embed each angle into its 2D representation $\vec{v}(\chi) = (\cos \chi, \sin \chi)$ and define the transport cost as:

$$W_{\text{torus}}(\mathcal{X}_0, \mathcal{X}_1) = \sum_{i,j} \Pi_{i,j}^{ang} \left\| \vec{v}(\chi_0^{(i)}) - \vec{v}(\chi_1^{(j)}) \right\|^2. \quad (13)$$

A neural network v_t^{ang} is trained using the permuted initialization $\mathcal{X}'_0 \sim \Pi^{ang}(\mathcal{X}_0, \mathcal{X}_1)$ to learn wrapped velocity vectors $\text{wrap}(\mathcal{X}_1 - \mathcal{X}'_0)$, where $\text{wrap}(\cdot)$ maps the angle difference into $(-\pi, \pi]$ to ensure minimal angular displacement.

During inference, we generate torsion trajectories via wrapped Euler integration:

$$\mathcal{X}'_{t+\Delta t} = (\mathcal{X}'_t + \Delta t \cdot v_t^{ang}(\mathcal{X}'_t; \theta)) \bmod 2\pi. \quad (14)$$

Summary of POTFlow

POTFlow unifies flow-based generative modeling across four distinct geometric spaces of peptide structure: Euclidean space for C_α positions, the rotation group $SO(3)$ for backbone orientations, the probability simplex for residue types, and the torus manifold for side-chain torsions. For each modality, we construct geometry-aware flow trajectories between noise and structure samples, initialized using structure-informed priors and refined via optimal transport to reduce path lengths.

The overall training objective minimizes the sum of squared velocity matching errors across all modalities, with tunable weights to balance the contribution of each component:

$$\mathcal{L}_{\text{total}} = \lambda_1 \cdot \text{Loss}_{\text{position}} + \lambda_2 \cdot \text{Loss}_{\text{orientation}} + \lambda_3 \cdot \text{Loss}_{\text{residue type}} + \lambda_4 \cdot \text{Loss}_{\text{torsion angle}}. \quad (15)$$

At inference time, POTFlow generates peptide structures by integrating learned velocity fields from OT-aligned initializations via Euler steps, adapted to the geometry of each space. This enables coherent, physically consistent peptide structure generation across all structural modalities. Training and generation procedures are summarized in Supplementary Algorithm E.

Metrics

For the peptide optimization task, our goal is to design models that can efficiently explore the hidden space around lead peptides. The following metrics are used for evaluation:

1. **Similarity** refers to the proportion of peptides that closely resemble the reference peptides, determined by two criteria: (a) a TM-score ≥ 0.5 [53, 54], and (b) a sequence identity ≥ 0.5 .
2. **Compactness** measures the variability in both the structural and sequence features, calculated as 1 minus the product of pairwise (1-TM-score) and (1-sequence identity) across all peptides generated for a given target.
3. **Affinity** evaluates the fraction of peptides that exhibit stronger binding affinities (or lower binding energies) compared to the native peptide.
4. **Stability** assesses the percentage of the generated complexes that are more thermodynamically stable (having lower total energy) than the native complexes, using the Rosetta energy function [55].
5. **RMSD (Root-Mean-Square deviation)** computes the discrepancy between the generated peptide structures and the native structures by analyzing the C_α distances after alignment.
6. **BSR (Binding site rate)** quantifies the similarity in peptide-target interactions by evaluating the overlap of the binding sites.

Baselines

We evaluate POTFlow against five powerful peptide design models. **RFDiffusion** [36] leverages pre-trained weights from RoseTTAFold [56] to generate protein backbone structures through a denoising diffusion process. The peptide sequences are subsequently reconstructed using **ProteinMPNN** [57]. **Protein-Generator** enhances RFDiffusion by incorporating joint sequence-structure generation [37]. **PepFlow** [25] generates full-atom peptides and samples them using a flow matching framework on a Riemannian manifold. **PepGLAD** [27] utilizes equivariant latent diffusion networks to generate full-atom peptide structures. **PepHAR** [35] generates peptide residues autoregressively, based on a learned prior distribution for hotspot residues.

Data and code availability

The data and code that support the findings of this study are available from the corresponding author upon reasonable request. All datasets and the complete codebase, including training and evaluation scripts, will be publicly released upon acceptance of the manuscript.

References

- [1] Stupp, R., Mason, W.P., Van Den Bent, M.J., Weller, M., Fisher, B., Taphoorn, M.J., Belanger, K., Brandes, A.A., Marosi, C., Bogdahn, U., *et al.*: Radiotherapy plus concomitant and adjuvant temozolomide for glioblastoma. *New England journal of medicine* **352**(10), 987–996 (2005)
- [2] Solinge, T.S., Nieland, L., Chiocca, E.A., Broekman, M.L.: Advances in local therapy for glioblastoma—taking the fight to the tumour. *Nature Reviews Neurology* **18**(4), 221–236 (2022)
- [3] Xu, G., Li, J.Y.: Atp5a1 and atp5b are highly expressed in glioblastoma tumor cells and endothelial cells of microvascular proliferation. *Journal of neuro-oncology* **126**, 405–413 (2016)
- [4] Watson, D., Bayik, D., Storevik, S., Moreino, S., Sprowls, S., Han, J., *et al.*: Mitochondria transfer enhances tumorigenicity in glioblastoma. *Cancer Discovery* **13**(7), 1512–1512 (2023) <https://doi.org/10.1158/2159-8290.CD-RW2023-080>

- [5] Craik, D.J., Fairlie, D.P., Liras, S., Price, D.: The future of peptide-based drugs. *Chemical biology & drug design* **81**(1), 136–147 (2013)
- [6] Henninot, A., Collins, J.C., Nuss, J.M.: The current state of peptide drug discovery: back to the future? *Journal of medicinal chemistry* **61**(4), 1382–1414 (2018)
- [7] Wang, L., Wang, N., Zhang, W., Cheng, X., Yan, Z., Shao, G., Wang, X., Wang, R., Fu, C.: Therapeutic peptides: current applications and future directions. *Signal transduction and targeted therapy* **7**(1), 48 (2022)
- [8] Giordano, C., Marchiò, M., Timofeeva, E., Biagini, G.: Neuroactive peptides as putative mediators of antiepileptic ketogenic diets. *Frontiers in neurology* **5**, 63 (2014)
- [9] Fosgerau, K., Hoffmann, T.: Peptide therapeutics: current status and future directions. *Drug discovery today* **20**(1), 122–128 (2015)
- [10] Davda, J., Declerck, P., Hu-Lieskovan, S., Hickling, T.P., Jacobs, I.A., Chou, J., Salek-Ardakani, S., Kraynov, E.: Immunogenicity of immunomodulatory, antibody-based, oncology therapeutics. *Journal for immunotherapy of cancer* **7**, 1–9 (2019)
- [11] Lefèvre, F., Rémy, M.-H., Masson, J.-M.: Alanine-stretch scanning mutagenesis: a simple and efficient method to probe protein structure and function. *Nucleic acids research* **25**(2), 447–448 (1997)
- [12] Quartararo, A.J., Gates, Z.P., Somsen, B.A., Hartrampf, N., Ye, X., Shimada, A., Kajihara, Y., Ottmann, C., Pentelute, B.L.: Ultra-large chemical libraries for the discovery of high-affinity peptide binders. *Nature communications* **11**(1), 3183 (2020)
- [13] Manning, M.C., Chou, D.K., Murphy, B.M., Payne, R.W., Katayama, D.S.: Stability of protein pharmaceuticals: an update. *Pharmaceutical research* **27**, 544–575 (2010)
- [14] Bhardwaj, G., Mulligan, V.K., Bahl, C.D., Gilmore, J.M., Harvey, P.J., Cheneval, O., Buchko, G.W., Pulavarti, S.V., Kaas, Q., Eletsky, A., *et al.*: Accurate de novo design of hyperstable constrained peptides. *Nature* **538**(7625), 329–335 (2016)
- [15] Bryant, P., Elofsson, A.: Evobind: in silico directed evolution of peptide binders with alphafold. *bioRxiv*, 2022–07 (2022)
- [16] Swanson, S., Sivaraman, V., Grigoryan, G., Keating, A.E.: Tertiary motifs as building blocks for the design of protein-binding peptides. *Protein Science* **31**(6), 4322 (2022)
- [17] Cao, L., Coventry, B., Goreshnik, I., Huang, B., Sheffler, W., Park, J.S., Jude, K.M., Marković, I., Kadam, R.U., Verschuere, K.H., *et al.*: Design of protein-binding proteins from the target structure alone. *Nature* **605**(7910), 551–560 (2022)
- [18] Bhat, S., Palepu, K., Hong, L., Mao, J., Ye, T., Iyer, R., Zhao, L., Chen, T., Vincoff, S., Watson, R., *et al.*: De novo design of peptide binders to conformationally diverse targets with contrastive language modeling. *bioRxiv*, 2023–06 (2023)
- [19] Chen, T., Dumas, M., Watson, R., Vincoff, S., Peng, C., Zhao, L., Hong, L., Pertsemliadis, S., Shapers-Cheu, M., Wang, T.Z., *et al.*: Pepmlm: target sequence-conditioned generation of therapeutic peptide binders via span masked language modeling. *ArXiv*, 2310 (2024)
- [20] Song, Y., Sohl-Dickstein, J., Kingma, D.P., Kumar, A., Ermon, S., Poole, B.: Score-based generative modeling through stochastic differential equations. *arXiv preprint arXiv:2011.13456* (2020)
- [21] Song, J., Meng, C., Ermon, S.: Denoising diffusion implicit models. *arXiv preprint arXiv:2010.02502* (2020)
- [22] Dhariwal, P., Nichol, A.: Diffusion models beat gans on image synthesis. *Advances in neural information processing systems* **34**, 8780–8794 (2021)
- [23] Lipman, Y., Chen, R.T., Ben-Hamu, H., Nickel, M., Le, M.: Flow matching for generative modeling.

- [24] Liu, X., Gong, C., Liu, Q.: Flow straight and fast: Learning to generate and transfer data with rectified flow. arXiv preprint arXiv:2209.03003 (2022)
- [25] Li, J., Cheng, C., Wu, Z., Guo, R., Luo, S., Ren, Z., Peng, J., Ma, J.: Full-atom peptide design based on multi-modal flow matching. arXiv preprint arXiv:2406.00735 (2024)
- [26] Lin, H., Zhang, O., Zhao, H., Jiang, D., Wu, L., Liu, Z., Huang, Y., Li, S.Z.: Ppflow: Target-aware peptide design with torsional flow matching. bioRxiv, 2024–03 (2024)
- [27] Kong, X., Jia, Y., Huang, W., Liu, Y.: Full-atom peptide design with geometric latent diffusion. arXiv preprint arXiv:2402.13555 (2024)
- [28] Wang, F., Wang, Y., Feng, L., Zhang, C., Lai, L.: Target-specific de novo peptide binder design with diffpepbuilder. Journal of Chemical Information and Modeling (2024)
- [29] Orengo, C.A., Todd, A.E., Thornton, J.M.: From protein structure to function. Current opinion in structural biology **9**(3), 374–382 (1999)
- [30] Li, K., Xu, Z., Mao, Y., You, P., Chen, L., Qi, Z.: Inhibition effect of DDIT4L and functional small peptides thereof on glioblastoma. CN Patent 112168969. Published Sept. 29, 2023 (2023). https://patentscope.wipo.int/search/zh/detail.jsf?docId=CN315173274&_cid=P10-MCTUUX-70760-4
- [31] You, P., Qi, Z.-X., Luo, H., Cai, B., Hu, X.-Y., Pan, J., Gan, P.-P., Zeng, X.-Y., Liao, R.-J., Tang, Q.-S., Yu, Y., Zhang, Z.-N., Yang, B.-J., Chen, L., Zhang, X., Li, K.-C., Mao, Y.: The ddit4l-tom40-atp5a pathway suppresses glioblastoma oncogenesis. bioRxiv (2025) <https://doi.org/10.1101/2025.07.27.666981>
- [32] Tong, A., Fatras, K., Malkin, N., Huguet, G., Zhang, Y., Rector-Brooks, J., Wolf, G., Bengio, Y.: Improving and generalizing flow-based generative models with minibatch optimal transport. arXiv preprint arXiv:2302.00482 (2023)
- [33] Wen, Z., He, J., Tao, H., Huang, S.-Y.: Pepbdb: a comprehensive structural database of biological peptide–protein interactions. Bioinformatics **35**(1), 175–177 (2019)
- [34] Wei, H., Wang, W., Peng, Z., Yang, J.: Q-biolip: A comprehensive resource for quaternary structure-based protein–ligand interactions. Genomics, Proteomics & Bioinformatics **22**(1) (2024)
- [35] Li, J., Chen, T., Luo, S., Cheng, C., Guan, J., Guo, R., Wang, S., Liu, G., Peng, J., Ma, J.: Hotspot-driven peptide design via multi-fragment autoregressive extension. arXiv preprint arXiv:2411.18463 (2024)
- [36] Watson, J.L., Juergens, D., Bennett, N.R., Trippe, B.L., Yim, J., Eisenach, H.E., Ahern, W., Borst, A.J., Ragotte, R.J., Milles, L.F., *et al.*: De novo design of protein structure and function with rfdiffusion. Nature **620**(7976), 1089–1100 (2023)
- [37] Lisanza, S.L., Gershon, J.M., Tipps, S., Arnoldt, L., Hendel, S., Sims, J.N., Li, X., Baker, D.: Joint generation of protein sequence and structure with rosettafold sequence space diffusion. bioRxiv, 2023–05 (2023)
- [38] Chen, Z., Peng, B., Zhai, T., Adu-Ampratwum, D., Ning, X.: Generating 3d small binding molecules using shape-conditioned diffusion models with guidance. Nature Machine Intelligence, 1–13 (2025)
- [39] Qian, H., Huang, W., Tu, S., Xu, L.: Kgdifff: towards explainable target-aware molecule generation with knowledge guidance. Briefings in Bioinformatics **25**(1), 435 (2024)
- [40] Salentin, S., Schreiber, S., Haupt, V.J., Adasme, M.F., Schroeder, M.: Plip: fully automated protein–ligand interaction profiler. Nucleic acids research **43**(W1), 443–447 (2015)
- [41] Ramachandran, G.N., Ramakrishnan, C., Sasisekharan, V.: Stereochemistry of polypeptide chain configurations. Journal of Molecular Biology **7**(1), 95–99 (1963) [https://doi.org/10.1016/S0022-2836\(63\)80023-6](https://doi.org/10.1016/S0022-2836(63)80023-6)

- [42] Andreatta, M., Alvarez, B., Nielsen, M.: Gibbscluster: unsupervised clustering and alignment of peptide sequences. *Nucleic Acids Research* **45**(W1), 458–463 (2017) <https://doi.org/10.1093/nar/gkx248> <https://academic.oup.com/nar/article-pdf/45/W1/W458/18137161/gkx248.pdf>
- [43] Abramson, J., Adler, J., Dunger, J., Evans, R., Green, T., Pritzel, A., Ronneberger, O., Willmore, L., Ballard, A.J., Bambrick, J., et al.: Accurate structure prediction of biomolecular interactions with alphafold 3. *Nature*, 1–3 (2024)
- [44] Bechinger, B., Zasloff, M., Opella, S.J.: Structure and orientation of the antibiotic peptide magainin in membranes by solid-state nuclear magnetic resonance spectroscopy. *Protein Science* **2**(12), 2077–2084 (1993)
- [45] Romeo, D., Skerlavaj, B., Bolognesi, M., Gennaro, R.: Structure and bactericidal activity of an antibiotic dodecapeptide purified from bovine neutrophils. *Journal of Biological Chemistry* **263**(20), 9573–9575 (1988)
- [46] Zasloff, M.: Antimicrobial peptides of multicellular organisms. *nature* **415**(6870), 389–395 (2002)
- [47] Cock, P.J., Antao, T., Chang, J.T., Chapman, B.A., Cox, C.J., Dalke, A., Friedberg, I., Hamelryck, T., Kauff, F., Wilczynski, B., et al.: Biopython: freely available python tools for computational molecular biology and bioinformatics. *Bioinformatics* **25**(11), 1422 (2009)
- [48] Villani, C.: Topics in Optimal Transportation vol. 58. American Mathematical Soc., ??? (2021)
- [49] Rao, S.S.: Engineering Optimization: Theory and Practice. John Wiley & Sons, ??? (2019)
- [50] Flamary, R., Courty, N., Gramfort, A., Alaya, M.Z., Boisbunon, A., Chambon, S., Chapel, L., Corenflos, A., Fatras, K., Fournier, N., Gautheron, L., Gayraud, N.T.H., Janati, H., Rakotomamonjy, A., Redko, I., Rolet, A., Schutz, A., Seguy, V., Sutherland, D.J., Tavenard, R., Tong, A., Vayer, T.: Pot: Python optimal transport. *Journal of Machine Learning Research* **22**(78), 1–8 (2021)
- [51] Hinde, J.: Logistic normal distribution. In: *International Encyclopedia of Statistical Science*, pp. 754–755. Springer, ??? (2011)
- [52] Atchison, J., Shen, S.M.: Logistic-normal distributions: Some properties and uses. *Biometrika* **67**(2), 261–272 (1980)
- [53] Zhang, Y., Skolnick, J.: Tm-align: a protein structure alignment algorithm based on the tm-score. *Nucleic acids research* **33**(7), 2302–2309 (2005)
- [54] Xu, J., Zhang, Y.: How significant is a protein structure similarity with tm-score= 0.5? *Bioinformatics* **26**(7), 889–895 (2010)
- [55] Chaudhury, S., Lyskov, S., Gray, J.J.: Pyrosetta: a script-based interface for implementing molecular modeling algorithms using rosetta. *Bioinformatics* **26**(5), 689–691 (2010)
- [56] Krishna, R., Wang, J., Ahern, W., Sturmfels, P., Venkatesh, P., Kalvet, I., Lee, G.R., Morey-Burrows, F.S., Anishchenko, I., Humphreys, I.R., et al.: Generalized biomolecular modeling and design with rosettafold all-atom. *Science* **384**(6693), 2528 (2024)
- [57] Dauparas, J., Anishchenko, I., Bennett, N., Bai, H., Ragotte, R.J., Milles, L.F., Wicky, B.I., Courbet, A., Haas, R.J., Bethel, N., et al.: Robust deep learning-based protein sequence design using proteinmpnn. *Science* **378**(6615), 49–56 (2022)
- [58] Weiss, N.A., Holmes, P.T., Hardy, M.: A Course in Probability. Pearson Addison Wesley, ??? (2006). <https://books.google.com/books?id=Be9fJwAACAAJ>
- [59] Mardia, K., Kent, J.: Bibby jm. multivariate analysis. New York: AcademicPress (1979)
- [60] Jumper, J., Evans, R., Pritzel, A., Green, T., Figurnov, M., Ronneberger, O., Tunyasuvunakool, K., Bates, R., Židek, A., Potapenko, A., et al.: Highly accurate protein structure prediction with alphafold. *nature* **596**(7873), 583–589 (2021)

Supplementary Materials for POTFlow

A Notes

Definition 1 We define a mapping function f_{DSSP} :

$$f_{\text{DSSP}}(\{\mathbf{x}_1^{(i,j)}\}_{j=1, i=1}^{N_{ss}, N_j}) \rightarrow \{g^{(j)}\}_{j=1}^{N_{ss}}, \quad (16)$$

where $f_{\text{DSSP}}(\mathbf{x}_1^{(i,j)}) = g^{(j)}$ specifies that the point $\mathbf{x}_1^{(i,j)}$ is mapped to the class $g^{(j)}$, and N_{ss} and N_j represents the number of secondary structures and the number of points in class $g^{(j)}$ respectively.

For each class $g^{(j)}$, we determine its centroid $\mathbb{C}_{g^{(j)}}$ by averaging the positions of all points assigned to $g^{(j)}$:

$$\mathbb{C}_{g^{(j)}} = \frac{1}{N_j} \sum_{i=1}^{N_j} \mathbf{x}_1^{(i,j)}. \quad (17)$$

Subsequently, we sample $\mathbf{x}_0^{(i,j)}$ from a Gaussian distribution centered at the centroid $\mathbb{C}_{g^{(j)}}$ with identity covariance:

$$\mathbf{x}_0^{(i,j)} \mid g^{(j)} \sim \mathcal{N}(\mathbb{C}_{g^{(j)}}, I_3). \quad (18)$$

Based on Definition 1 and the proposed initialization, we can directly derive the following propositions:

Proposition 1 (Rotation Equivariance) *The sampling scheme in Definition 1 is **rotation equivariant**, meaning that for any rotation matrix $R \in SO(3)$, if we rotate the original data points by R , the newly sampled points also rotate by R accordingly.*

Proposition 2 (Improved Initialization via Class-Specific Centroids) *Class-Specific Initialization yields a lower or equal average squared distance compared to Global Initialization. Let $\mathbb{C}_{\text{global}}$ denote the global centroid of all points:*

$$\mathbb{C}_{\text{global}} = \frac{1}{N} \sum_{i=1}^N \mathbf{x}_1^{(i)}. \quad (19)$$

Define two initialization schemes for new points $\mathbf{x}_0^{(i,j)}$ and $\mathbf{x}_0^{(i)}$ respectively:

1. **Class-Specific:** $\mathbf{x}_0^{(i,j)} \mid g^{(j)} \sim \mathcal{N}(\mathbb{C}_{g^{(j)}}, I_3)$.
2. **Global:** $\mathbf{x}_0^{(i)} \sim \mathcal{N}(\mathbb{C}_{\text{global}}, I_3)$.

Then, the Class-Specific Initialization minimizes the average squared Euclidean distance between \mathbf{x}_0 and the original points \mathbf{x}_1 compared to the Global Initialization. Formally,

$$\frac{1}{N} \sum_{j=1}^{N_{ss}} \sum_{i=1}^{N_j} \mathbb{E} \left[\|\mathbf{x}_0^{(i,j)} - \mathbf{x}_1^{(i,j)}\|^2 \right] \Big|_{\text{Class-Specific}} \leq \frac{1}{N} \sum_{i=1}^N \mathbb{E} \left[\|\mathbf{x}_0^{(i)} - \mathbf{x}_1^{(i)}\|^2 \right] \Big|_{\text{Global}}.$$

Theorem 3 (*Shorter Paths via Class-Specific + OT Couplings*) *Let $\mathcal{X} \subset \mathbb{R}^d$ be the ambient space of a particular modality (e.g., C_α -positions in Euclidean space). Suppose we have:*

$$q_1(\mathbf{x}_1) : \text{target distribution}, q_0^{(\text{vanilla})}(\mathbf{x}_0) : \text{vanilla prior}.$$

We define:

$$q_0^{(\text{ours})}(\mathbf{x}_0')$$

to be the class-specific plus OT-based prior, constructed by (1) centering initialization per class (Proposition 2) and (2) coupling those initialization points to the data points via an optimal transport policy Π^* . Then

$$W^2(q_0^{(\text{ours})}, q_1) \leq W^2(q_0^{(\text{vanilla})}, q_1),$$

where $W^2(\cdot, \cdot)$ denotes the Wasserstein-2 (or geodesic) transport cost,¹ and the inequality is strict if the vanilla prior $q_0^{(\text{vanilla})}$ differs sufficiently from $q_0^{(\text{ours})}$.

¹In Euclidean space, $W^2(p, q) = \inf_{\Pi \in \Gamma(p, q)} \mathbb{E}_{(\mathbf{x}, \mathbf{y}) \sim \Pi} \|\mathbf{x} - \mathbf{y}\|^2$. In manifolds such as $SO(3)$ or \mathbb{T}^k , we replace $\|\cdot\|^2$ by the corresponding geodesic-squared distance.

A.1 Proof of Proposition 1

Proof 1. Invariance of Class Labels Under Rotation. By assumption, the class labels $\{g^{(j)}\}$ (e.g., secondary structure types) are determined by intrinsic properties such as local geometric configurations. Therefore, applying a uniform rotation $R \in SO(3)$ to all data points does not alter their class memberships. Formally, if $x_1^{(i,j)} \in g^{(j)}$, then $Rx_1^{(i,j)} \in g^{(j)}$.

2. Transformation of Centroids Under Rotation. After applying rotation R to each point in class $g^{(j)}$, the new centroid $\tilde{\mathbb{C}}_{g^{(j)}}$ becomes

$$\tilde{\mathbb{C}}_{g^{(j)}} = \frac{1}{N_j} \sum_{i=1}^{N_j} Rx_1^{(i,j)} = R \left(\frac{1}{N_j} \sum_{i=1}^{N_j} x_1^{(i,j)} \right) = R\mathbb{C}_{g^{(j)}}.$$

Thus, the centroid undergoes the same rotation R .

3. Rotation Invariance of Isotropic Gaussian Distributions. Each new point $x_0^{(i,j)}$ is sampled from

$$x_0^{(i,j)} = \mathbb{C}_{g^{(j)}} + \epsilon^{(i,j)},$$

where $\epsilon^{(i,j)} \sim \mathcal{N}(\mathbf{0}, I_3)$. Since the covariance matrix I_3 is isotropic, it remains unchanged under rotation. Therefore, for any $R \in SO(3)$,

$$R\epsilon^{(i,j)} \sim \mathcal{N}(\mathbf{0}, I_3).$$

This implies that the distribution of the noise term $\epsilon^{(i,j)}$ is rotation invariant.

4. Overall Rotation Equivariance of the Sampling Scheme. Suppose the entire dataset is rotated by $R \in SO(3)$. The rotated centroid is $\tilde{\mathbb{C}}_{g^{(j)}} = R\mathbb{C}_{g^{(j)}}$, and the rotated noise term is $\tilde{\epsilon}^{(i,j)} = R\epsilon^{(i,j)}$. The newly sampled point after rotation is

$$\tilde{x}_0^{(i,j)} = \tilde{\mathbb{C}}_{g^{(j)}} + \tilde{\epsilon}^{(i,j)} = R\mathbb{C}_{g^{(j)}} + R\epsilon^{(i,j)} = R \left(\mathbb{C}_{g^{(j)}} + \epsilon^{(i,j)} \right) = Rx_0^{(i,j)}.$$

Therefore, the sampling scheme satisfies

$$\tilde{x}_0^{(i,j)} = Rx_0^{(i,j)},$$

which aligns with the definition of rotation equivariance. \square

A.2 Proof of Proposition 2

Proof To compare the two initialization schemes, we compute the expected squared Euclidean distance between the initialized points x_0 and the original points x_1 under both schemes.

1. Class-Specific Initialization:

$$x_0^{(i,j)} = \mathbb{C}_{g^{(j)}} + \epsilon^{(i,j)},$$

where $\epsilon^{(i,j)} \sim \mathcal{N}(\mathbf{0}, I_3)$.

The squared distance is:

$$\|x_0^{(i,j)} - x_1^{(i,j)}\|^2 = \|\mathbb{C}_{g^{(j)}} - x_1^{(i,j)} + \epsilon^{(i,j)}\|^2.$$

Expanding the square and taking expectation:

$$\mathbb{E} \left[\|x_0^{(i,j)} - x_1^{(i,j)}\|^2 \right] = \|\mathbb{C}_{g^{(j)}} - x_1^{(i,j)}\|^2 + \mathbb{E} \left[\|\epsilon^{(i,j)}\|^2 \right] + 2\mathbb{E} \left[(\mathbb{C}_{g^{(j)}} - x_1^{(i,j)})^\top \epsilon^{(i,j)} \right].$$

Since $\epsilon^{(i,j)}$ has zero mean and is independent of $x_1^{(i,j)}$,

$$\mathbb{E} \left[(\mathbb{C}_{g^{(j)}} - x_1^{(i,j)})^\top \epsilon^{(i,j)} \right] = 0.$$

Also, $\mathbb{E} \left[\|\epsilon^{(i,j)}\|^2 \right] = \text{trace}(I_3) = 3$. Therefore,

$$\mathbb{E} \left[\|x_0^{(i,j)} - x_1^{(i,j)}\|^2 \right] = \|\mathbb{C}_{g^{(j)}} - x_1^{(i,j)}\|^2 + 3.$$

Taking the average over all points:

$$\begin{aligned} \frac{1}{N} \sum_{j=1}^{N_{ss}} \sum_{i=1}^{N_j} \mathbb{E} \left[\|x_0^{(i,j)} - x_1^{(i,j)}\|^2 \right]_{\text{Class-Specific}} &= \frac{1}{N} \sum_{j=1}^{N_{ss}} \sum_{i=1}^{N_j} \left(\|\mathbb{C}_{g^{(j)}} - x_1^{(i,j)}\|^2 + 3 \right) \\ &= \frac{1}{N} \sum_{j=1}^{N_{ss}} \sum_{i=1}^{N_j} \|\mathbb{C}_{g^{(j)}} - x_1^{(i,j)}\|^2 + 3. \end{aligned}$$

2. Global Initialization:

$$x_0^{(i)} = \mathbb{C}_{\text{global}} + \epsilon^{(i)},$$

where $\epsilon^{(i)} \sim \mathcal{N}(\mathbf{0}, I_3)$.

Similarly,

$$\mathbb{E} \left[\|x_0^{(i)} - x_1^{(i)}\|^2 \right] = \|\mathbb{C}_{\text{global}} - x_1^{(i)}\|^2 + 3.$$

Taking the average over all points:

$$\begin{aligned} \frac{1}{N} \sum_{i=1}^N \mathbb{E} \left[\|x_0^{(i)} - x_1^{(i)}\|^2 \right]_{\text{Global}} &= \frac{1}{N} \sum_{i=1}^N \left(\|\mathbb{C}_{\text{global}} - x_1^{(i)}\|^2 + 3 \right) \\ &= \frac{1}{N} \sum_{i=1}^N \|\mathbb{C}_{\text{global}} - x_1^{(i)}\|^2 + 3. \end{aligned}$$

3. Comparing the Two Schemes:

To show that Class-Specific Initialization yields a smaller average squared distance, it suffices to show:

$$\frac{1}{N} \sum_{j=1}^{N_{ss}} \sum_{i=1}^{N_j} \|\mathbb{C}_{g^{(j)}} - x_1^{(i,j)}\|^2 \leq \frac{1}{N} \sum_{i=1}^N \|\mathbb{C}_{\text{global}} - x_1^{(i)}\|^2.$$

This follows from the **Law of Total Variance** [58] or the **Within-Class Sum of Squares Minimization** in clustering.

Lemma 1 Let $\{x_1^{(i,j)}\}$ be partitioned into classes $\{g^{(j)}\}$. Then,

$$\frac{1}{N} \sum_{j=1}^{N_{ss}} \sum_{i=1}^{N_j} \|\mathbb{C}_{g^{(j)}} - x_1^{(i,j)}\|^2 \leq \frac{1}{N} \sum_{i=1}^N \|\mathbb{C}_{\text{global}} - x_1^{(i)}\|^2.$$

Proof of Lemma Consider the decomposition of variance:

$$\frac{1}{N} \sum_{i=1}^N \|x_1^{(i,j)} - \mathbb{C}_{\text{global}}\|^2 = \frac{1}{N} \sum_{j=1}^{N_{ss}} \sum_{i=1}^{N_j} \|x_1^{(i,j)} - \mathbb{C}_{g^{(j)}}\|^2 + \frac{1}{N} \sum_{j=1}^{N_{ss}} N_j \|\mathbb{C}_{g^{(j)}} - \mathbb{C}_{\text{global}}\|^2.$$

This is known as the **Total Sum of Squares (TSS)** [59] decomposition into **Within-Cluster Sum of Squares (WCSS)** and **Between-Cluster Sum of Squares (BCSS)**:

$$\text{TSS} = \text{WCSS} + \text{BCSS}.$$

Since $\text{BCSS} \geq 0$, it follows that:

$$\text{WCSS} \leq \text{TSS}.$$

Therefore,

$$\frac{1}{N} \sum_{j=1}^{N_{ss}} \sum_{i=1}^{N_j} \|x_1^{(i,j)} - \mathbb{C}_{g^{(j)}}\|^2 \leq \frac{1}{N} \sum_{i=1}^N \|x_1^{(i)} - \mathbb{C}_{\text{global}}\|^2.$$

□

Adding the constant term 3 to both sides preserves the inequality:

$$\frac{1}{N} \sum_{j=1}^{N_{ss}} \sum_{i=1}^{N_j} \left(\|\mathbb{C}_{g^{(j)}} - x_1^{(i,j)}\|^2 + 3 \right) \leq \frac{1}{N} \sum_{i=1}^N \left(\|\mathbb{C}_{\text{global}} - x_1^{(i)}\|^2 + 3 \right).$$

Hence,

$$\frac{1}{N} \sum_{j=1}^{N_{ss}} \sum_{i=1}^{N_j} \mathbb{E} \left[\|x_0^{(i,j)} - x_1^{(i,j)}\|^2 \right] \Big|_{\text{Class-Specific}} \leq \frac{1}{N} \sum_{i=1}^N \mathbb{E} \left[\|x_0^{(i)} - x_1^{(i)}\|^2 \right] \Big|_{\text{Global}}.$$

□

A.3 Proof of Theorem 3

Proof We prove this in three stages:

Step 1: Class-Specific Centers Reduce Within-Class Distances.

By Proposition 2 in the main text, partitioning data points into secondary-structure classes and centering the initialization $\mathbf{x}_0^{(i,j)}$ around *class-specific* centroids $\mathbb{C}_{g^{(j)}}$ lowers the expected squared distance to the target $\mathbf{x}_1^{(i,j)}$ compared with using a *global* centroid. Concretely:

$$\mathbb{E} \left[\|\mathbf{x}_1^{(i,j)} - \mathbf{x}_0^{(\text{class})}\|^2 \right] \leq \mathbb{E} \left[\|\mathbf{x}_1^{(i,j)} - \mathbf{x}_0^{(\text{global})}\|^2 \right],$$

and summing over all classes and residues yields a strictly smaller or equal total distance.

Step 2: OT Coupling Minimizes Transport Cost.

Recall that the Wasserstein-2 distance can be written as an infimum over all couplings Π with marginals q_0 and q_1 . The *optimal* transport coupling Π^* exactly minimizes

$$\mathbb{E}_{(\mathbf{x}_0, \mathbf{x}_1) \sim \Pi} \|\mathbf{x}_1 - \mathbf{x}_0\|^2.$$

Hence, using Π^* to re-initialize \mathbf{x}'_0 *must* yield a smaller expected distance to data than any naive (e.g., i.i.d.) pairing.

Step 3: Combining Both for a Tighter Prior.

- **Class-Specific Initialization** ensures each $\mathbf{x}_0^{(i,j)}$ starts closer to $\mathbf{x}_1^{(i,j)}$ within its semantic or structural class than a global scheme would.
- **OT Coupling** then permutes/rearranges these points to optimally match them to the data distribution, further lowering the transport cost.
- **Resulting Improvement:** the distribution $q_0^{(\text{ours})}$ of these re-initialized \mathbf{x}'_0 satisfies

$$W^2(q_0^{(\text{ours})}, q_1) \leq W^2(q_0^{(\text{class})}, q_1) \leq W^2(q_0^{(\text{vanilla})}, q_1).$$

Thus, our initialization strategy is strictly closer (in the Wasserstein sense) to q_1 than a vanilla prior, yielding *shorter probability paths* for Flow Matching. \square

Corollary 3.1 (Efficiency of Flow Matching) *The reduced Wasserstein distance enables:*

- Fewer ODE steps T for comparable sample quality
- Lower variance in vector field estimation
- Higher fidelity and coverage, since less “unnecessary traveling” occurs in high-dimensional spaces.

B Toy Examples

B.1 Global Initialization VS Class-Specific Initialization

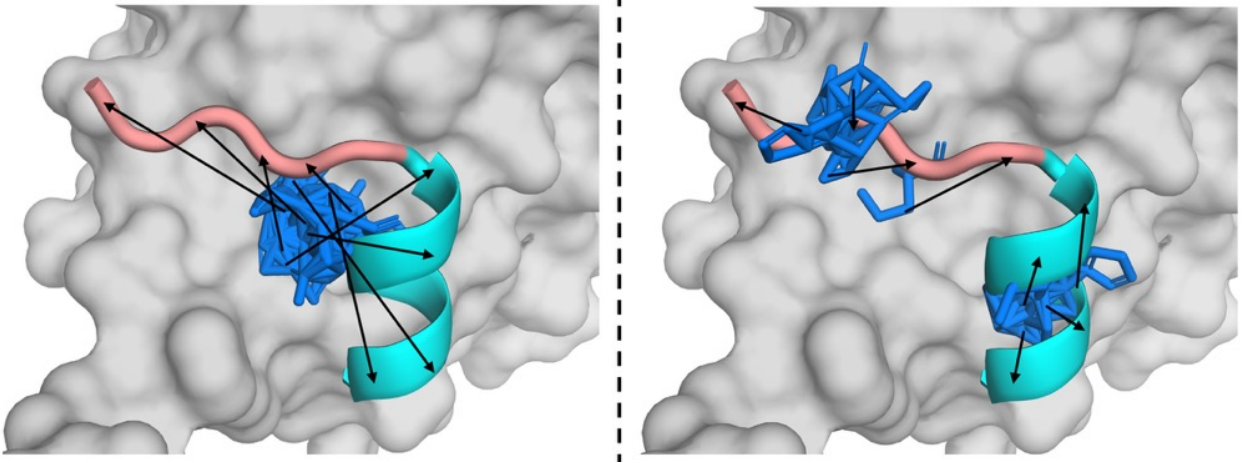


Fig. 1 Comparison between global initialization (left) and class-specific initialization (right). The black arrows indicate the flow velocity vectors. As proved in Supplementary Notes A.2, the flow trajectories in the right diagram are shorter than those in the left diagram.

B.2 Optimal Transport between 2D Empirical Distributions

As illustrated in Fig. 2, the trajectories in the right image show fewer cross-interactions than those in the left image. In flow matching models, ODE trajectories should not intersect during training. If they do, the model may learn a vector field that represents a compromise between the intersecting trajectories, blending their directions. This ambiguity in the vector field can prevent the model from accurately capturing the true flow dynamics, resulting in poor generalization and inaccurate behavior at the intersection points.

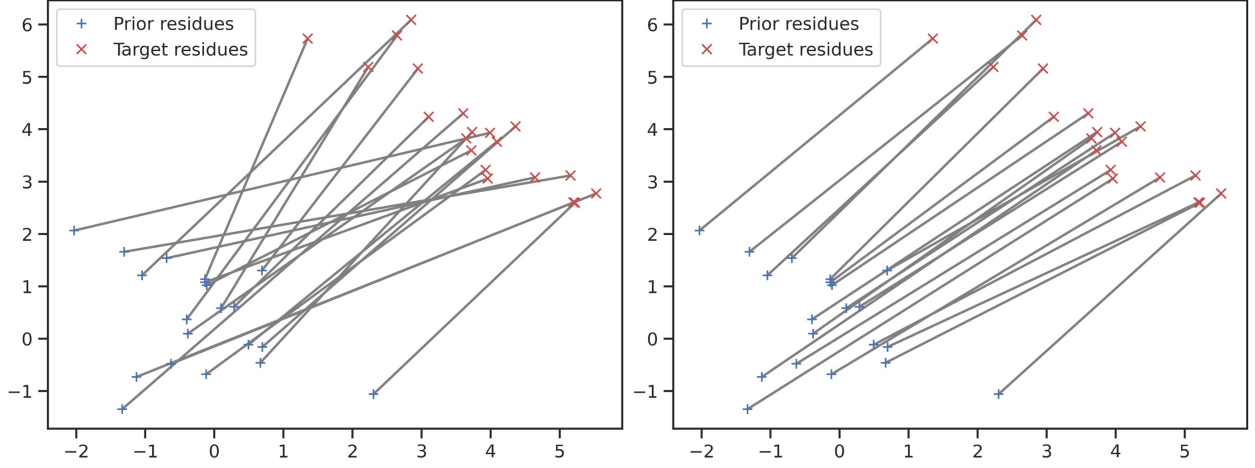


Fig. 2 A toy example using 2D points to illustrate the different flow trajectories before (left) and after (right) applying the optimal transport plan.

C Classification of Peptide Secondary Structures

Fig. 3 presents the empirical cumulative distribution function (ECDF) of the total number of secondary-structure elements (helices, β -strands, turns, etc.) per peptide candidate. The steep rise between 3 and 6 elements shows that most peptides contain 3–6 secondary-structure features, with the cumulative proportion approaching unity as the count increases. Besides, as illustrated in Table 1, we list the eight DSSP secondary-structure codes and their definitions, which we have consolidated into three primary categories: Type 0 (helical structures: H, G, I), Type 1 (strand structures: B, E), and Type 2 (turn/coil structures: T, S, –). This grouping preserves the main helix and strand classes while combining all flexible or unstructured segments into a single category to facilitate subsequent statistical analyses.

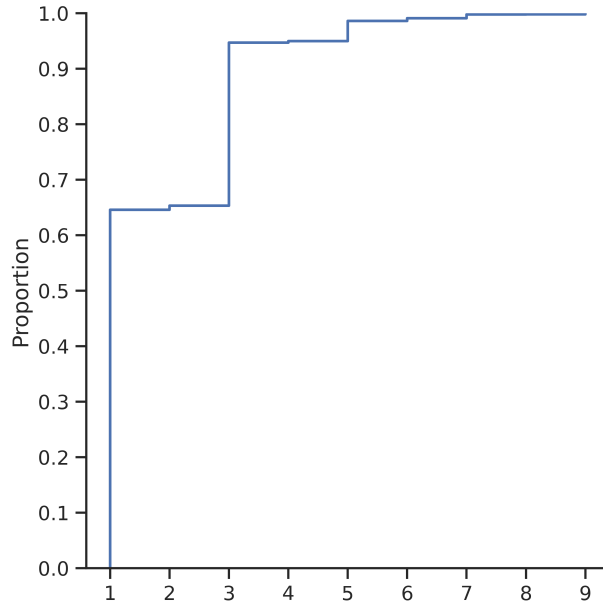


Fig. 3 Empirical Cumulative Distribution Function (ECDF) analysis of the distribution of secondary structure counts in individual peptides.

Code	Structure	Type Index
H	Alpha helix	0
B	Isolated beta-bridge residue	1
E	Strand	1
G	3-10 helix	0
I	Pi helix	0
T	Turn	2
S	Bend	2
-	None	2

Table 1 Eight types of secondary structures. For simplicity, we consolidate these into three primary categories, designated as 0, 1, and 2.

D Experiment Setup

D.1 Model Architecture

Our flow model is primarily developed based on the guidelines set forth in PepFlow [25] and the Invariant Point Attention (IPA) architecture as detailed by Jumper et al. [60], which utilizes both the provided features and the structural frames of the backbone. This model employs an invariant attention mechanism to analyze the interactions between the receptor protein and the peptide backbone currently under consideration.

Here, we give a detailed description of the model architecture.

Input Definitions

Given a protein structure consisting of N residues and a batch size of B , the input to the encoder includes:

- Discrete amino acid sequence types $\text{seq}_i \in \{1, \dots, 22\}$.
- Scalar timestep t used in denoising diffusion models.
- Side chain torsion angles $\boldsymbol{\theta}_i \in \mathbb{R}^5$ ($\chi_1, \chi_2, \chi_3, \chi_4, \chi_5$).
- Rigid-body transformations ($\mathbf{R}_i^{(0)}, \mathbf{t}_i^{(0)}$) for each residue i .

NodeEmbedder

For each residue i :

$$\mathbf{h}_i^{\text{init}} = \text{MLP}_{\text{node}}([e_i^{\text{aa}} \parallel e_i^{\text{crd}} \parallel e_i^{\text{dihed}}]) \in \mathbb{R}^{d_s},$$

where:

- e_i^{aa} is the learned embedding of the amino-acid type.
- e_i^{crd} are the local (C_α -frame) atom coordinates flattened by one-hot selection.
- e_i^{dihed} is the angular encoding of (ϕ, ψ, ω) .

The output is masked by whether the C_α exists.

EdgeEmbedder

For each residue pair (i, j) :

$$\mathbf{z}_{ij}^{(0)} = \text{MLP}_{\text{edge}}([e_{ij}^{\text{aapair}} \parallel e_{ij}^{\text{relpos}} \parallel e_{ij}^{\text{dist}} \parallel e_{ij}^{\text{dihed}}]) \in \mathbb{R}^{d_z},$$

where:

- e_{ij}^{aapair} embeds the pair of residue types.
- e_{ij}^{relpos} embeds their relative sequence offset (clamped).
- e_{ij}^{dist} projects Gaussian-kernelized inter-atomic distances.
- e_{ij}^{dihed} encodes the two inter-residue dihedrals.

The output is masked to same-chain residue pairs.

Initial Feature Mixing

For each residue i , fuse node, sequence, timestep and angle embeddings:

$$\mathbf{H}_i^{(0)} = \text{MLP}\left([\mathbf{h}_i^{\text{init}} \parallel \mathbf{s}_i \parallel \mathbf{t}_i \parallel \mathbf{a}_i]\right) \in \mathbb{R}^{d_s},$$

where:

- \mathbf{s}_i is the learned embedding of the *current* amino-acid at step t .
- \mathbf{t}_i is the time-step embedding.
- \mathbf{a}_i is the angular encoding of the sampled torsions.
- \parallel denotes concatenation.

Iterative Block Updates

Let B denote the total number of blocks. Each block $b = 0, \dots, B-1$ performs the following computations:

$$\Delta \mathbf{H}_i^{\text{IPA}} = \text{IPA}^{(b)}(\mathbf{H}_i^{(b)}, \mathbf{Z}_{ij}^{(b)}, (\mathbf{R}_i^{(0)}, \mathbf{t}_i^{(0)})),$$

Transformer Sequence Attention

The output of IPA is combined with a skip connection and passed through a Transformer encoder:

$$\mathbf{X}_i^{(b)} = \text{LayerNorm}(\mathbf{H}_i^{(b)} + \Delta \mathbf{H}_i^{\text{IPA}}), \quad (20)$$

$$\mathbf{X}_i^{(b)} = \text{TransformerEncoder}^{(b)}(\mathbf{X}_i^{(b)}), \quad (21)$$

$$\mathbf{H}_i^{(b+1)} = \text{MLP}(\mathbf{H}_i^{(b)} + \text{Linear}(\mathbf{X}_i^{(b)})). \quad (22)$$

Feedforward Transition and Rigid Update

Node features are further processed and used to compute rigid-body updates:

$$\Delta \mathbf{r}_i^{(b)} = \text{RigidUpdate}(\mathbf{H}_i^{(b+1)}), \quad (23)$$

$$(\mathbf{R}_i^{(b+1)}, \mathbf{t}_i^{(b+1)}) = (\mathbf{R}_i^{(b)}, \mathbf{t}_i^{(b)}) \circ \Delta \mathbf{r}_i^{(b)}, \quad (24)$$

where \circ denotes the composition of rigid transformations.

Edge Feature Update

For all blocks except the last, edge embeddings are updated:

$$\mathbf{Z}_{ij}^{(b+1)} = \text{EdgeTransition}(\mathbf{H}_i^{(b+1)}, \mathbf{Z}_{ij}^{(b)}). \quad (25)$$

Final Output Predictions

After B blocks of iteration, the final outputs include:

$$\hat{\mathbf{R}}_i = \mathbf{R}_i^{(B)}, \quad (26)$$

$$\hat{\mathbf{t}}_i = \mathbf{t}_i^{(B)}, \quad (27)$$

$$\hat{\boldsymbol{\theta}}_i = \text{AngleNet}(\mathbf{H}_i^{(B)}) \bmod 2\pi, \quad (28)$$

$$\hat{\mathbf{p}}_i = \text{SeqNet}(\mathbf{H}_i^{(B)}), \quad (29)$$

where $\hat{\mathbf{R}}_i$ and $\hat{\mathbf{t}}_i$ define the predicted rigid-body transformation of residue i , $\hat{\boldsymbol{\theta}}_i$ denotes the predicted side chain torsion angles, and $\hat{\mathbf{p}}_i$ is the predicted amino acid probability distribution.

D.2 Training

The distinctions between the three models are specified as follows: the class priors are omitted in the **POTFlow w/o class prior**; the **POTFlow w/o OT** is characterized by the exclusion of the optimal transport policy; and **POTFlow** represents the comprehensive model that incorporates all features, including the optimal transport policy and the class prior. The parameters are set as follows: $\lambda_1 = 0.5, \lambda_2 = 0.5, \lambda_3 = 1.0, \lambda_4 = 1.0$.

Each of these models undergoes training on four NVIDIA A100 GPUs, employing a Distributed Data Parallel (DDP) training framework over 2 million iterations. We maintain a learning rate of 5×10^{-4} and configure the batch size to 16 for each GPU in the distributed setup.

D.3 Sampling

The sampling process is conducted on a single NVIDIA A100 GPU, utilizing 200 timesteps during the Euler step update. For each protein in the test set, we concurrently sample 64 peptides.

E Pseudocode

We outlined the overall training and sampling procedures here.

Algorithm 1 POTFlow Training Procedure

- 1: **Input:** Peptide dataset $D = \{(\mathcal{P}^i, \mathcal{G}_1^i)\}_{i=1}^n$, where \mathcal{P}^i represents the protein target and \mathcal{G}^i represents the peptide.
 - 2: **while** not converged **do**
 - 3: Sample a protein-peptide pair $(\mathcal{P}^i, \mathcal{G}_1^i)$ from the dataset and a noise peptide \mathcal{G}_0^i from the multimodal prior distributions.
 - 4: Compute the multimodal transport policy Π for the pair $(\mathcal{G}_0^i, \mathcal{G}_1^i)$ using Equation (2), (5), (9), and (13), then sample a new noise peptide $\mathcal{G}_0^{i'}$ from the policy Π .
 - 5: Sample $t \sim U(0, 1)$, and compute a noisy peptide $\mathcal{G}_t^{i'}$ by interpolating between $\mathcal{G}_0^{i'}$ and the target peptide \mathcal{G}_1^i .
 - 6: Compute the flow vector fields for the interpolated peptide $\mathcal{G}_t^{i'}$ using the neural network $v_t(\mathcal{G}_t^{i'}, \mathcal{P}; \theta)$.
 - 7: Compute the loss function \mathcal{L}_θ^{all} using Eq. (15) and update the model parameters θ accordingly.
 - 8: **end while**
 - 9: **Return:** Final model parameters θ .
-

Algorithm 2 POTFlow Sampling Procedure

- 1: **Input:** The lead peptide \mathcal{G}_l and its binding target protein \mathcal{P} .
 - 2: Initialize \mathcal{G}_0 from the multimodal prior distributions.
 - 3: Compute optimal transport map Π between the peptide pair $(\mathcal{G}_0, \mathcal{G}_l)$.
 - 4: Sample $\mathcal{G}_0' \sim \Pi$.
 - 5: **for** $t = 0$ **to** 1 **step** $\frac{1}{T}$ **do**
 - 6: Calculate the flow vector fields predicted by the neural network $v_t(\mathcal{G}_t', \mathcal{P}; \theta)$.
 - 7: Update the noisy peptide \mathcal{G}_t' by the Euler methods in Equation (3), (6), (10) and (14).
 - 8: **end for**
 - 9: **Return:** Final generated peptides \mathcal{G}_1' .
-

F Visualization

As shown in Fig. 4, we selected six peptides of different lengths from the test set for visualization. We found that shorter peptides closely match the lead peptide in sequence, which correlates with lower RMSD values. In contrast, longer peptides demonstrate increased sequence diversity and higher RMSD values, a reasonable outcome given their greater degrees of freedom.

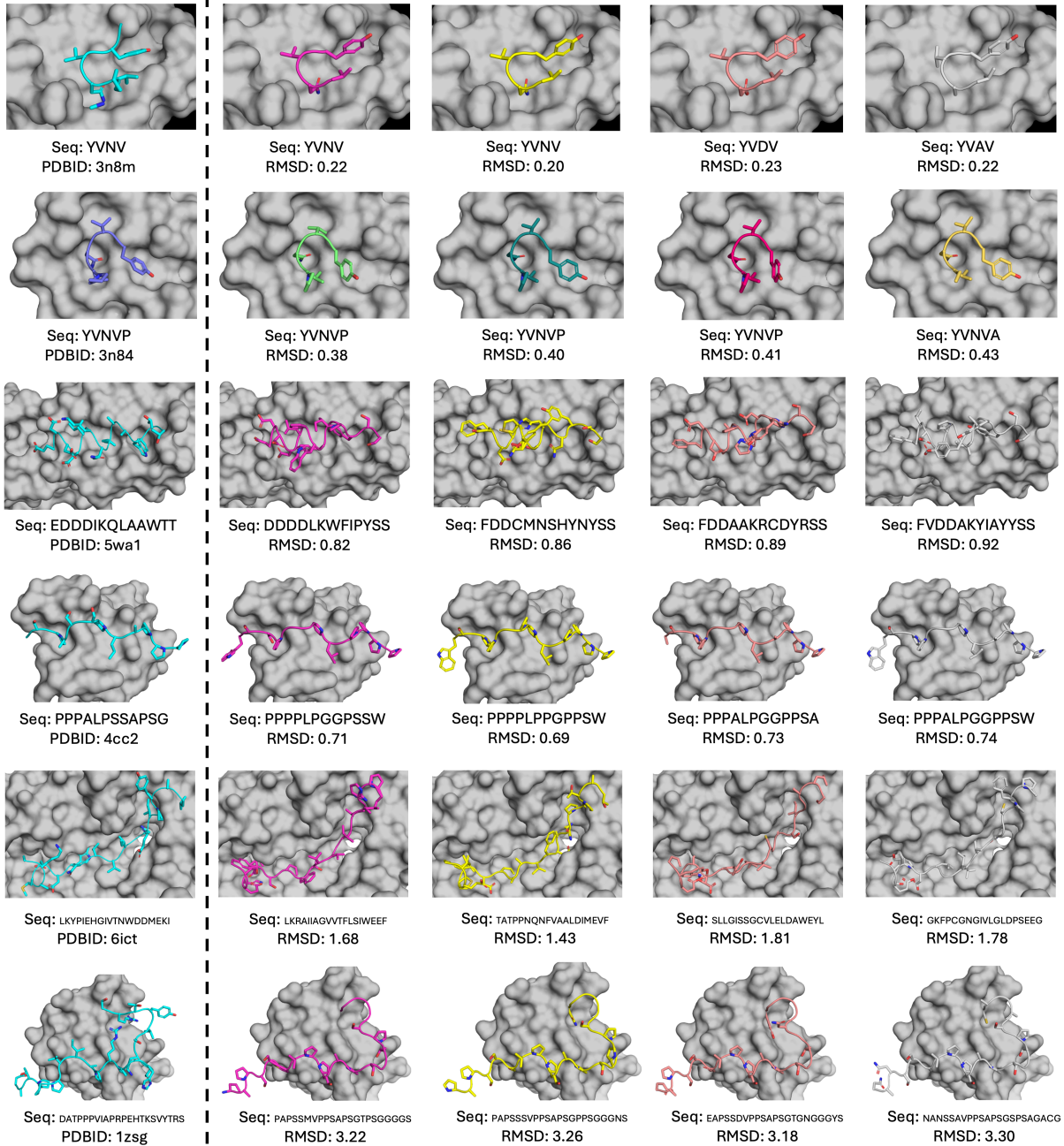


Fig. 4 Visualization of peptides generated by POTFlow. The left column displays the lead peptide, whereas the right four columns showcase the peptides our method generated. We choose peptides of different lengths for our visualization. The first two rows have the shorter peptides, the middle two rows show peptides of a medium length, and the final two rows are made up of the longer peptides.

G ATP Concentrations in Different Cell Lines

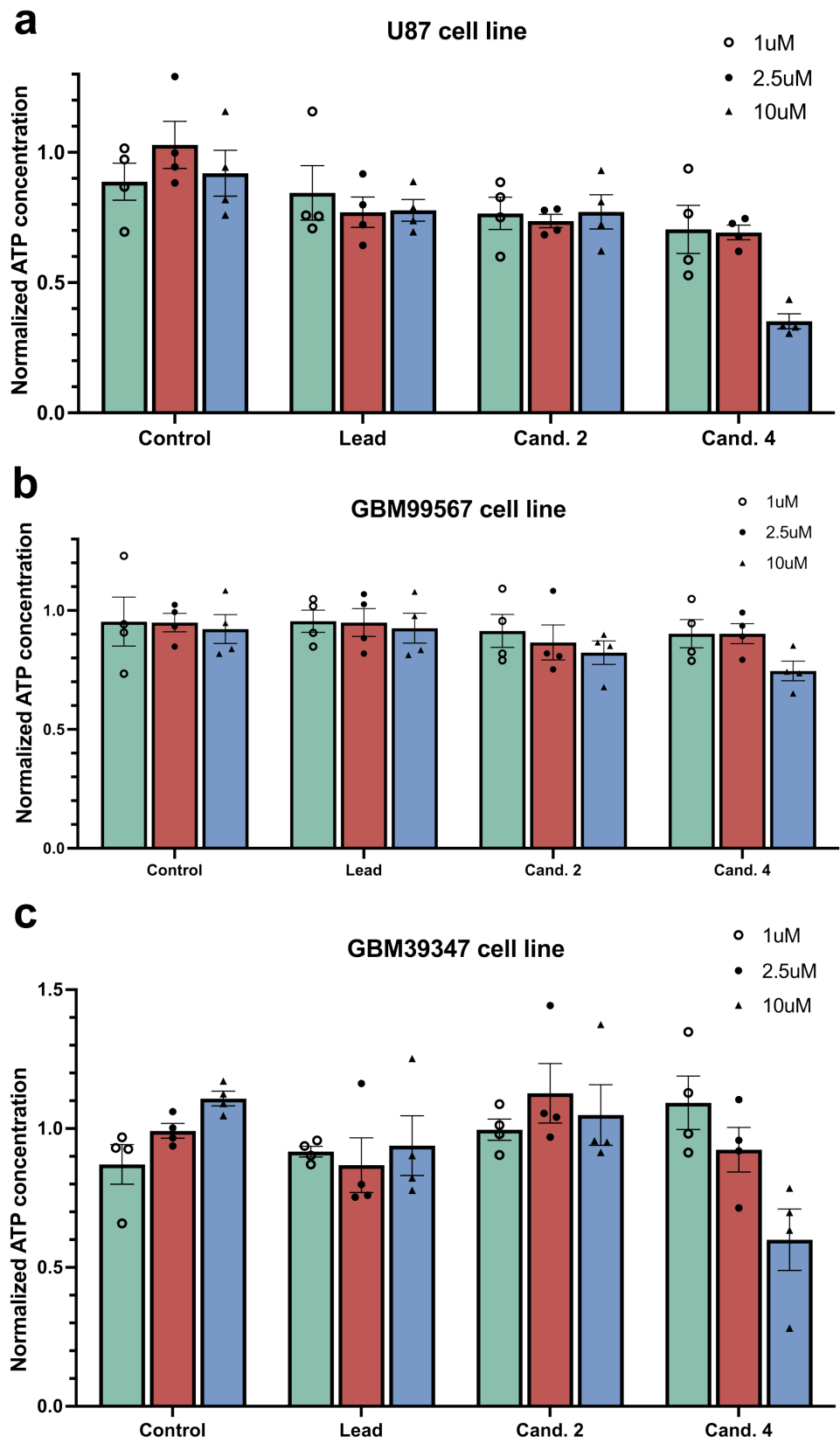


Fig. 5 ATP concentrations in GBM cell lines (U87, 99567, and 39347) treated for 4 hours with control, the lead peptide, Cand.2, and Cand.4 at concentrations of 1.0 μ M (open circles), 2.5 μ M (filled circles), and 10 μ M (triangles).

H Inhibition of Viability Rate

Cell line	1 μ M			2.5 μ M			10 μ M		
	Lead	Cand. 4	IVR %	Lead	Cand. 4	IVR %	Lead	Cand. 4	IVR %
Cell line 293 (non-cancerous)	0.60	0.54	10.00%	0.57	0.50	12.28%	0.56	0.52	7.14%
Cell line 99567 (GBM)	1.01	0.79	21.78%	0.71	0.59	16.90%	0.57	0.18	68.42%
Cell line U87 (GBM)	0.55	0.45	18.18%	0.54	0.46	14.81%	0.53	0.40	24.53%

Table 2 We summarize the cell viability measurements for the lead peptide and Cand. 4 across three cell lines (including one non-cancerous and two GBM cell lines) at three concentration levels (1, 2.5, and 10 μ M). The inhibition of viability rate (IVR%) is computed to quantify the enhanced inhibitory effect of Cand. 4 over the lead peptide, defined as the relative reduction in viability. $IVR = \frac{Viability_{Lead} - Viability_{Cand. 4}}{Viability_{Lead}} \times 100\%$.

I Log-rank Test in PDX Model

Groups	p-value
Control vs Low dose	0.2325
Low dose vs High dose	0.4302
Control vs High dose	0.0198*

Table 3 Log-rank test results comparing survival curves between groups. * represent s statistically significant at the 0.05 level.